PRODUCTION AND CHARACTERIZATION OF NANOSTRUCTURED SILICON CARBIDE

by

KENDRA LEE WALLIS

Bachelor of Science, 1985
West Texas A & M University
Canyon, Texas

Master of Science, 1993
The University of Texas at Arlington
Arlington, Texas

Submitted to the Graduate Faculty of the
College of Science and Engineering
Texas Christian University
in partial fulfillment of the requirements
for the degree of

Doctor of Philosophy

May 2008

Acknowledgments

To my husband Mike, thanks for your love and support. To my two beautiful daughters, Megan and Zoe, may you have the opportunity to fulfill all your dreams.

Thanks to Dr. Waldek Zerda from whom I have learned how to be an independent researcher, as well as how to mentor graduate students.

Additional thanks to the following:

Jerry Kachinska, the electronics technician, Jaime Cuanzon in the glass shop, Mike Murdock and David Yale in the machine shop. Monika Weiligor, Stephen Nauyoks, and Ryan Rich, the graduate students in our group, and Mirza Hasan, undergraduate lab student.

David Robertson and Sid Richardson Carbon Black Co.

Svitlana Stelmach and others in Poland who are co-authors in my first publication. Jaromir Patyk (Jarek) who is co-author on my second publication.

At Hitachi High Technologies: Thanks to Michael Bain, Kevin Cronyn, and Bill Roth.

Contents

Vita

Abstract

List of Figures

List of Tables

Chapter 1

Introduction

Production of nano-structured materials is currently an active area of research. It has been shown that some mechanical properties, such as hardness and toughness, increase with decreasing grain size in some materials[1]. One possible explanation is that the increased surface area of the smaller grains provides greater resistance to strain and to fracture. Breaking nanosize particles requires a lot of energy due to the formation of the surface. Although stacking faults are common in nanostructures, high energy defects are not[2]. This results in greater resistance to fracture because a crack would have to meander around nanograins instead of cleaving along a defect. In addition, nanostructured materials often have improved thermal, electrical, and optical properties. It has been demonstrated that the size of nanomaterials and the structure of the outer layers determine their mechanical, electrical, and optical properties.[1] Manufacturing processes must produce nanosize materials of uniform dimensions and of strictly controlled surfaces to find practical applications. All the observed differences in properties are related to the nanostructure itself, and thus precise control of the structure in terms of size, surface, shape, and defects remains the goal of much of the current research. Ultimately though, the structure of materials on the nanoscale is poorly understood.

As the study of nanomaterials continues, more methods of production are discovered and refined, and the list of observed properties of these new materials that are unique to the nanostructured domain continues to grow. In fact, however, there is a lack of understanding of the mechanisms by which these interesting structures form and why they demonstrate such unique and often improved physical and mechanical properties. Composites containing nanomaterials are often stronger, harder, more electrically conductive, more thermally conductive, more of or better than whatever property their larger-structured material equivalents possess. The key to understanding the difference must lie in understanding the formation of the nanostructure since the structure produces the difference in properties.

Semiconductor materials are of special interest due to their electronic and optical properties, and ceramics are of special interest due to their physical and mechanical properties. Silicon carbide fits into both categories, being a wide band-gap semiconductor and a ceramic with hardness nearly equal to that of diamond. The research presented here describes discoveries that are important contributions to understanding not only the structure of silicon carbide nanotubes and nanowires, but the reaction mechanism involved in producing them.

Finding the reaction mechanism involves watching progression of the reaction in time and characterizing the evolution of morphology and structure. In order to study and determine the nanostructure of produced SiC, it is necessary to produce reasonably large quantities of high purity silicon carbide nanowires. A mixture of the same reactants used in the first method of production here was used in a previous kinetics study under high-temperature high-pressure conditions.[3] In those experiments, it was determined by SEM (Scanning Electron Microscopy) and HRTEM (High Resolution Transmission Electron Microscopy) that the product formed was silicon carbide in the form of nanowires mixed with nanograins and other nanostructures. It was not possible to separate the nanowires for exclusive study.

In this study, silicon carbide nanowires were produced reliably by two different methods: heating a mixture in an induction furnace for short times at different temperatures; and sintering separated precursors in a tube furnace for longer times at one temperature, while varying the precursors. In both cases, the product was then heated in air to oxidize and thus remove excess carbon while forming silica (silicon dioxide) from excess silicon. It was demonstrated that samples containing silica could be washed in a potassium hydroxide solution in order to remove the silica if necessary. These post-treatment methods were done in order to be certain that high purity silicon carbide could be acquired by removing any excess reactants.

The second method of production proved to be an excellent manufacturing process by which large quantities of pure SiC nanowires could be produced. The method is simple and easily reproduced as well as being relatively inexpensive.

This report is divided into six chapters. This chapter provides an introduction to the research, including motivation, and an overview of the topics discussed. Chapter 2 includes a description of the methods of sample preparation, the initial reactants used, and the experimental methods used to produce and characterize nanostructured SiC. In Chapter 3, theoretical reaction kinetics is described in more detail, followed by the results of this kinetics study of nanostructured SiC and discussion of the reaction mechanism inferred from the results. Chapter 4 describes the morphology of the products and methods used in characterization of the product followed by Chapter 5, which details the micro- and nano- structure results of the study, including methods used to determine structure. Conclusions are discussed in Chapter 6, and the experimental results are connected to theoretically predicted structures and growth mechanisms. Lastly, the future work suggested by these results is described.

Chapter 2

Experimental Methods

2.1 Sample Preparation

2.1.1 Nanosize Reactants

It is well-known that particle size not only affects reaction rates, but also physical and mechanical properties of a substance. Decreasing the particle size of a reactant, increases its surface area, which may increase the reaction rate and create a product with small grain size. This is the basis for nanocomposite technology, which seeks to develop high-performance materials for engineering applications.[1]

Carbon nanotubes were first observed experimentally by Iijima[4] using transmission electron microscopy (TEM). Nanotubes represent one-dimensional systems in which the four valence electrons of carbon exhibit a modified sp^2 hybridization of atomic orbitals. This is rather unusual because although in carbon, three hybridizations are possible, other Group IV elements such as silicon and germanium exhibit primarily sp^3 hybridization. In two dimensions, sp^2 hybridization of carbon forms graphite, and in three-dimensions, sp^3 hybridization forms the tetrahedral structure of diamond. For the zero-dimensional phase of carbon known as fullerene, a closed polyhedra of 60 carbon atoms resembling a soccer ball is formed. The endcaps of nanotubes are hemispheres of a fullerene.[5]

Although multi-wall nanotubes (MWNT) were the first to be observed[4], direct measurement on individual shells is difficult. Thus most of the experimentally measured properties of nanotubes are done on single-wall nanotubes (SWNT). A single-wall nanotube is a cylindrical graphene sheet with diameter 1 to 10 nm. The graphene sheet is composed of six-membered carbon rings in a honeycomb lattice.

A MWNT consists of multiple concentric cylindrical shells with a common axis. The outer shells contribute to the strength of the nanotube, making MWNTs ideal for adding strength and fracture toughness. One promising use of carbon nanotubes is reinforcement in ceramic and metal-matrix composites. The increased strength offered by the addition of nanotubes may represent increased fracture toughness.[1] Reactions involving MWNTs are the focus of this study. It is clear, however, that these results would be enhanced by a detailed study using SWNTs. Although one sample was produced using SWNT for comparison, a detailed study will be left for future study.

2.1.2 Induction Furnace Samples

The first reliable method of producing SiC nanowires used in this study is a modification of the work done by Wang.[3] An induction furnace was used to heat a mixture of silicon nanopowder and carbon multiwalled nanotubes (MWNTs). Reactants used in the mixture were silicon nanopowder, APS (average particle size) 30 nm, and carbon multiwalled nanotubes, outer diameters 60-100 nm and length 5-15 μm, both purchased from Nanostructured and Amorphous Materials, Inc. The nanoparticles were mixed in a 3:1 Si:C molar ratio by dispersion in acetone and high energy sonication with an ultrasonic processor (Sonic & Materials, Inc.) at 60 W. After mixing, excess liquid was evaporated from the mixture.

This is the same method of mixing used in previous studies of these reactants under high-pressure high-temperature conditions.[3] In those experiments, a conventional furnace was used for heating, which heated the samples slowly, and the error in reaction time measurements was on the order of hours. Induction heating reduced the error in reaction time to seconds, providing data to determine reaction rates and find the activation energy of this reaction much more accurately.

Prior to heating using the induction furnace, many experiments were done to find the preferred set-up and the most appropriate crucible size and material. Some of that initial work is presented in Chapter 3. For the final induction experiments, samples of the SiC mixture were measured and poured into a tantalum crucible and compressed with constant force. The crucible was placed on a ceramic stage inside a quartz tube. Air in the tube was evacuated to 10^{-3} mbar and the sample was heated by induction.

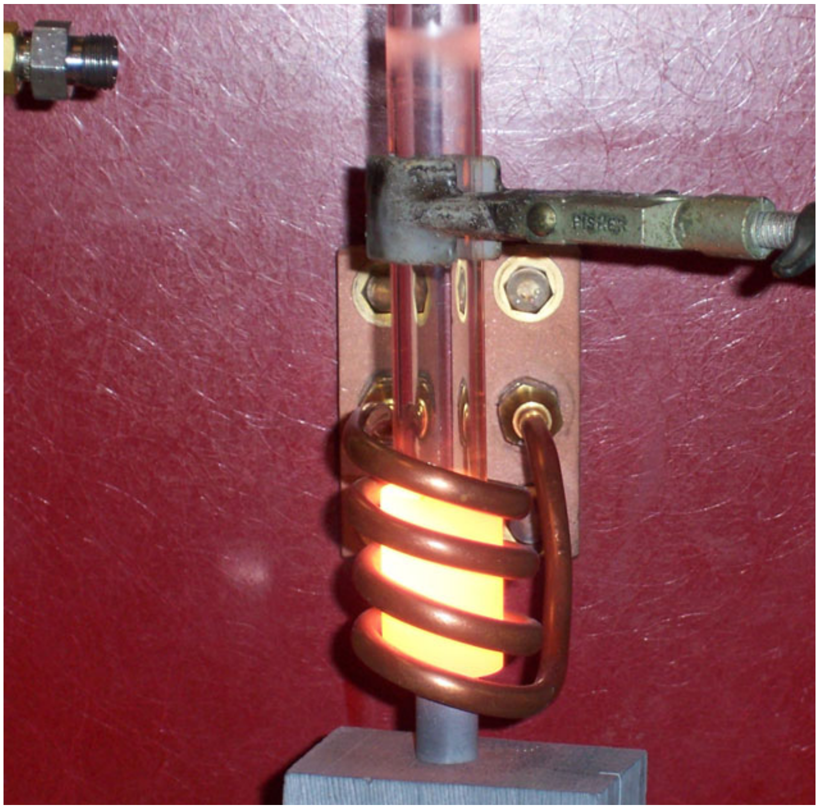

Figure 2.1: Alternating current in the coil creates an alternating magnetic field, which induces an opposing current in the conductive metal placed inside the coil. As the current switches direction, energy is lost to heating the metal inside according to Joule's law.

Heating of the mixture was done in an induction furnace using the Inductoheat Statipower BSP12 power supply with a custom-made coil in vacuum. The Statipower BSP12 operates at maximum power 25 kW and frequency 30 kHz. Frequency is maintained at 30 kHz and current to the coil is adjusted to control temperature of the sample inside. High frequency alternating current through the coil creates a changing magnetic field, which induces eddy currents in the tantalum crucible. Figure 2.1 shows the glowing crucible inside the coil in the experimental set-up. The quartz tube was held inside the cylindrical coil such that the sample was near the center of the induced field. Most of the energy is lost to the tantalum by Joule heating which in turn heats the sample inside the crucible. Temperature was measured by a thermocouple placed inside the crucible and inserted into the sample mixture.

Each induction furnace sample was examined by x-ray diffraction (XRD), which was used to determine concentration of produced SiC. The SiC mass concentration was determined from comparison of x-ray peak intensity. Peaks [111] of SiC and [111] of Si were used for the induction furnace samples. The relationship of peak intensity to mass concentration was determined experimentally. Although there was unreacted carbon in some samples, which was removed by burning in air at temperature 700°C, one can expect that SiC will not be burned, and excess Si will be oxidized. The presence of carbon nanotubes in the samples does not influence the relative intensity of peaks used for the calculation of SiC concentration, which was confirmed by XRD measurements done before and after burning.

One of the major advantages to induction heating over other methods of heating is the ability to reach a constant temperature in a known amount of time repeatedly. Since induction heating is established as a stable process, measurements of equilibrium temperatures reached at different input power should produce a reliable means of finding temperature. Rapid and stable heating makes induction heating far superior to slower methods as a means of measuring reaction rate. However, this method was still unable to produce pure nanowires, and as described below, the removal of excess silicon is difficult, tedious, and not reliable.

2.1.3 Tube Furnace Samples

In describing the results, the SiC nanotubes and nanowires produced by this method will be referred to as the tube furnace samples. For most of these vapor phase experiments, SiC was obtained from silicon powder, particle size less than 44 μm, purchased from Sigma-Aldrich, and MWNTs obtained from two different sources. Tube furnace samples A were made using the same MWNTs used in making the induction furnace samples, tangled MWNTs purchased from Nanostructured and Amorphous Materials, Inc. Nano-Labs supplied aligned MWNTs of diameter 30 nm ± 15 nm and length 1 - 5 μm (tube furnace samples B). Both suppliers used the same preparation technique - chemical vapor deposition. In addition, one sample was produced from SWNT and one from carbon nanograss.

Carbon nanograss (CNG) is another nanostructure where individual sticks of carbon are grown in alignment perpendicular to a substrate such that their morphology resembles a field of freshly cut grass. The sticks or blades of grass have diameters in the nanometer range and lengths that may grow to more than 100 nm.[6, 7] Researchers have focused on controlling the orientation of carbon nanotubes in order to align them, especially for electronic applications, with some success.[8, 9, 10] Silicon carbide nanograss would be useful in a wide range of semiconductor technologies, as well as applications for hard ceramic nanocomposites, providing motivation for the use of CNG as a precursor in these experiments. Although SiC nanograss did not form under these conditions, further enhancements to the method and a more detailed study of nanograss formation would certainly be worthwhile.

In this set of experiments, all samples but one were sintered in a conventional tube furnace with the reactants initially separated. One sample was sintered in a large conventional furnace as discussed below. To keep the solid reactants separated, initially one small quartz tube was split into two boats, one containing carbon and one containing silicon powder, as shown in Figure 2.2.

It was found after a few experiments using two boats that static electricity in these very light particles caused the MWNTs to escape the open boat easily, thus losing mass and allowing mixing of the precursors before beginning the experiments. The procedure was then modified so that the MWNTs were placed in a small quartz tube open only at one end (the boat) and the silicon powder was left loose in a larger quartz tube into which the boat containing MWNTs

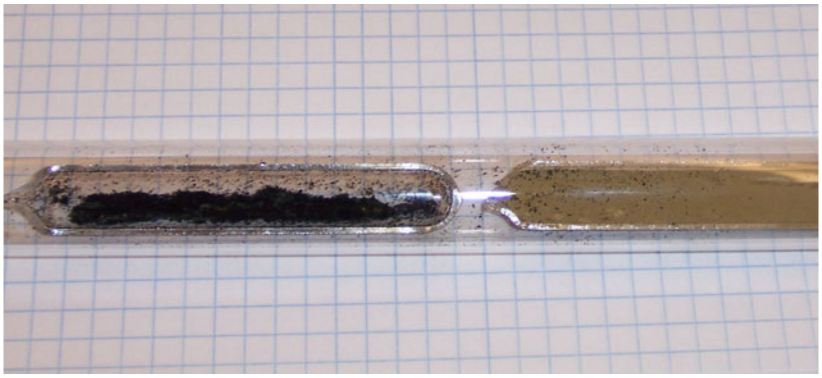

Figure 2.2: Initial configuration for tube furnace experiments using two quartz boats to keep reactants separated.

was placed. By this method, it was much easier to control the amount of starting material and to control separation of precursors. Air was evacuated from the outer quartz tube, pressure 10^{-3} mbar, and the tube was sealed.

The sealed ampoule was then heated uniformly in a tube furnace to sintering temperature of 1200°C to allow the silicon to sublime and disperse throughout the ampoule. The temperature was held constant at 1200°C for all samples, and the reaction was continued for varying reaction times in order to study the progression of the reaction in time. In addition, samples were sintered using different forms of carbon as a precursor in order to examine structure and morphology differences in the produced silicon carbide.

Sample names, sintering times, starting material, and posttreatment burning temperatures are shown in Table 2.1. The sample names are first either TF, for those samples sintered in the tube furnace or CF, for the one sample that was sintered in the conventional furnace. Next, the sample is given a name representing the precursor carbon that was used where A refers to the tangled MWNTs, B refers to the aligned MWNTs, SWNT refers to the sample produced from singlewalled nanotubes, and CNG refers to the sample produced from carbon nanograss. The number following the letters represents the number of hours that the sample was sintered. The molar ratio of silicon to carbon was 2:1 and the precursor silicon powder was micron sized with the exception of Sample CFA64, which is described next.

Sample Name	Precursor C	Reaction Time (h)	Burning Temp(°C)
$TFA1$	$MWNTA$	1	1050
$TFA2$	$MWNTA$	2	1050
$TFA3$	$MWNTA$	3	1050
$TFA4$	$MWNTA$	4	700
$TFA6$	$MWNTA$	6	700
$TFA8$	$MWNTA$	8	700
$TFB20$	$MWNTB$	20	700
$TFB26$	$MWNTB$	26	700
$TFSWNT26$	$SWNT$	26	700
$TFCNG26$	CNG	26	700
$CFA64$	$MWNTA$	64	700

Table 2.1: All samples sintered in the tube furnace with the precursor carbon used, reaction time, and post-treatment burning temperature. Precursor MWNT A are tangled nanotubes, MWNT B are aligned nanotubes, SWNT are single walled nanotubes, and CNG is carbon nanograss.

Sample CFA64 was an early attempt at making nanowires by this method. Starting materials were silicon nanopowder and carbon MWNTs A. The mass of each reactant was not measured, but was estimated to be 12 times more silicon than carbon by volume, approximating a 3:1 molar ratio of Si:C. The ampoule containing sample CFA64 was sintered in a conventional furnace for 64 hours. Sample TFB20 is the only sample that was preheated in the conventional oven at 1000°C for 20 hours. Visually, there was no evidence of any reaction, and further analysis has produced no evidence that this preheating had any effect on the produced SiC nanowires. The sample was then heated in the tube furnace to 1200°C, in the same way as the other tube furnace samples, for approximately 20 hours. The molar ratio was 2:1 Si:C, with measured amounts 0.5000 g Si and 0.1069 g MWNT B. Sample TFB26 was prepared at the same time as TFB20 with the same molar ratio and same mass measurements using the same precursors (MWNT B), without preheating in the conventional furnace. It was heated in the tube furnace to 1200°C and held for 26 hours. Comparison of the structures produced in TFB20, TFB26, and CFA64 is discussed in Chapter 5.

For the tube furnace samples, the reaction occurred at the surface of the carbon and thus the boat containing produced SiC also contained unreacted carbon, but unreacted silicon remained separate, thus eliminating the need to remove excess silicon from the product. The presence of β-SiC and excess MWNT was confirmed by XRD measurements. To remove traces of unreacted carbon nanotubes, the SiC specimens were heated in air for 2 hours in order to obtain pure SiC for the study of morphology (see Chapter 4) and structure (see Chapter 5). Carbon reacted with oxygen and after heating no carbon structures were detected in x-ray diffractograms. By this method, SiC nanotubes and nanowires were produced without nanograins as were produced from the induction furnace samples described above.

X-ray diffraction confirmed that carbon also vaporized and some SiC was present in the remaining Si. In addition, XRD confirmed that all samples in Table 2.1 produced SiC, including those using SWNT and carbon nanograss precursors, and experiments at lower temperatures showed that SiC was produced by this method at temperatures as low as 850°C. Further detailed study of those results are left for future experiments, and would most certainly contribute important additional information to the current literature.

Separate experiments were carried out to determine the optimum temperature for heating to oxidize and remove unreacted carbon. It is is desirable that post-treatment burning be done at lower temperature and for a shorter time in order to reduce or eliminate any effects that the burning might impose on the SiC product formed. This would reduce the chance of incurring unwanted contamination or further unwanted reactions in the samples. Initially, MWNTs were burned in air at lower temperatures for set burning time of 2 hours. The temperature was then increased incrementally, and the mass measured to determine the percentage of carbon lost at each temperature. The results of these experiments are shown in Table 2.2. From that study, it was determined that 700°C was the lowest temperature required to efficiently eliminate excess carbon by oxidation in 2 hours.

After determining that minimum temperature 700°C would reduce the amount of carbon by 45%, some of the samples were burned at higher temperatures. A time analysis of burning

t (min)	T (°C)	Mass (g)	Mass Lost (g)	Percentage (%)
0	40	4.6316	0.0000	0.00
120	300	4.5643	0.0673	1.45
120	400	4.5202	0.1114	2.41
120	500	4.1611	0.4705	10.2
120	600	3.6122	1.0194	22.0
120	700	2.5423	2.0893	45.1
120	1050	0.0000	2.5423	100.0

Table 2.2: Carbon MWNTs were burned for 2 hours at 5 different temperatures to determine the minimum temperature for post-treatment burning. At 1050°C, all the carbon was eliminated in 2 hours.

at 1050°C was also done and verified that a minimum of 2 hours was required at the higher temperature to ensure elimination of all excess carbon. A comparison was made between samples burned at 700°C and 1050°C, and no differences in product formed or excess carbon removed were found. All post-treatment burning was done in air for 2 hours as shown in Table 2.2. Figure 2.3 demonstrates the comparison, and it can be seen that there are no obvious differences in morphology caused by burning at different temperatures. Raman spectrographs and x-ray diffractograms also confirm this conclusion and will be discussed later. Because burning at 1050°C was was more invasive and more likely to produce undesirable effects on the structure, most samples were burned at 700°C. Those samples were then tested by x-ray diffraction to confirm that no carbon peaks were detected, ensuring that this temperature was sufficient for the purpose at hand.

2.1.4 High Purity SiC Nanowires

For an in-depth study of SiC nanowires, it was necessary to first determine that it was possible to obtain high purity SiC nanowires reliably. The mixture of nanostructures obtained in high-temperature high-pressure experiments using the same precursors as the induction furnace samples[3] provided motivation for modifying the manufacturing process. The method for producing high purity silicon carbide nanowires from the induction furnace samples involved first producing silicon carbide with excess reactants and then removing the excess. This procedure was tested and the results are shown in Figure 2.4. (a) is the x-ray diffraction spectra for a 1:3 Si:C molar ratio mixture of the precursors used in the induction furnace samples dispersed in acetone by high energy sonication using an ultrasonic processor and then evaporated.

The mixture was sintered for 2 minutes in a nitrogen atmosphere using the induction furnace operating at input power 6.65 kW. Temperature was not measured directly, but the input power setting indicates that the temperature just reached 1200°C in the 2 minute sintering time. Silicon carbide was produced as shown in Figure 2.4(b). Some of both reactants remained, which allowed testing the method of removing excess reactants.

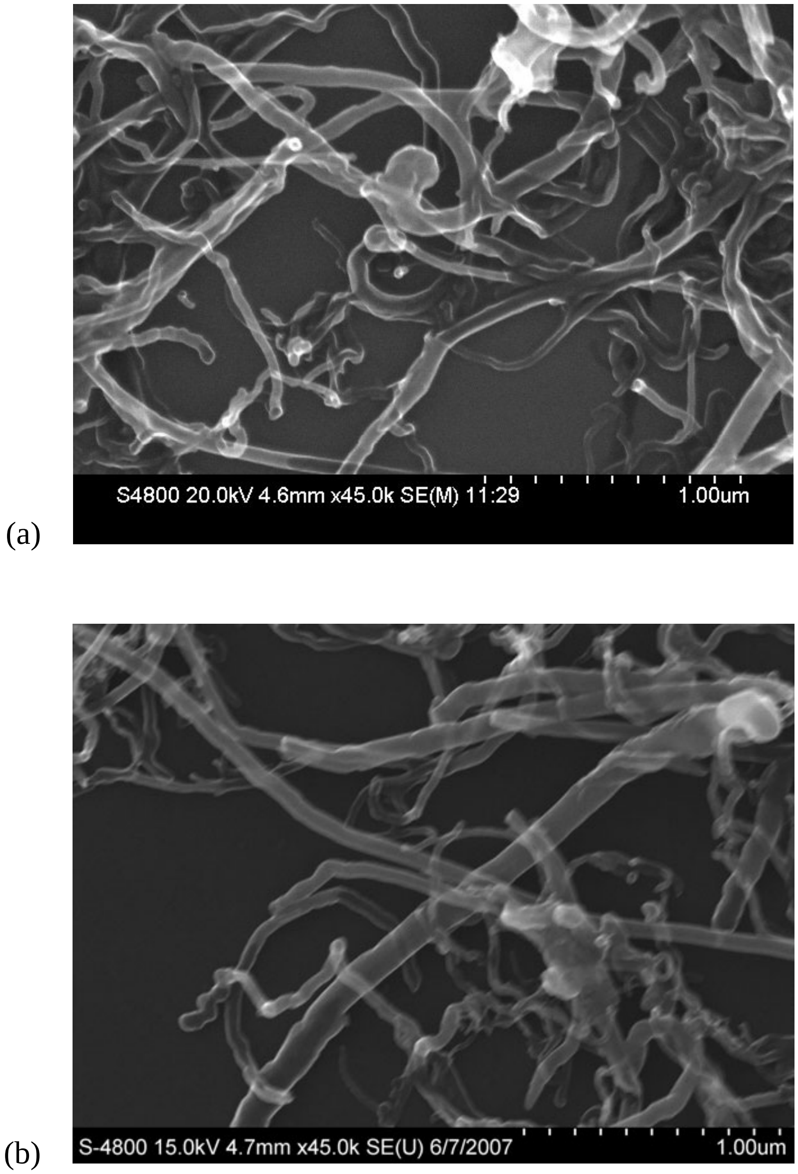

Figure 2.3: High resolution SEM images of samples (a) TFA3, burned at 1050°C and (b) TFA4, burned at 700°C, show no difference in morphology resulted from post-treatment burning at different temperatures

Carbon was removed by burning in an oven at 700°C for 2 hours. In Figure 2.4(c) essentially no carbon remains, indicating that burning was successful. Post-treatment heating in air was successful in oxidizing silicon, so the sample was washed with a 30% solution of potassium hydroxide (KOH) to eliminate most, if not all, excess silica.

Washing was done over several days of agitating, allowing the solid to settle completely, removing liquid from the top, adding distilled water, and repeating. The success of the method is shown in Figure 2.4(d). Although this last figure appears to have more "noise," this is only because the peak of SiC is small compared to excess carbon and silicon in previous spectra. It was shown that this method can be used to remove excess reactants with confidence.

In addition to the success of this method to remove excess of both reactants, the vapor-phase experiments done using the tube furnace samples required only the removal of excess carbon, which was easily done by burning in air. Any unreacted silicon in the tube furnace remained separated from the boat containing the produced SiC and any excess carbon. The high-purity SiC nanowires obtained from the tube furnace samples allowed the further study of morphology and growth without the work involved in removing excess silicon.

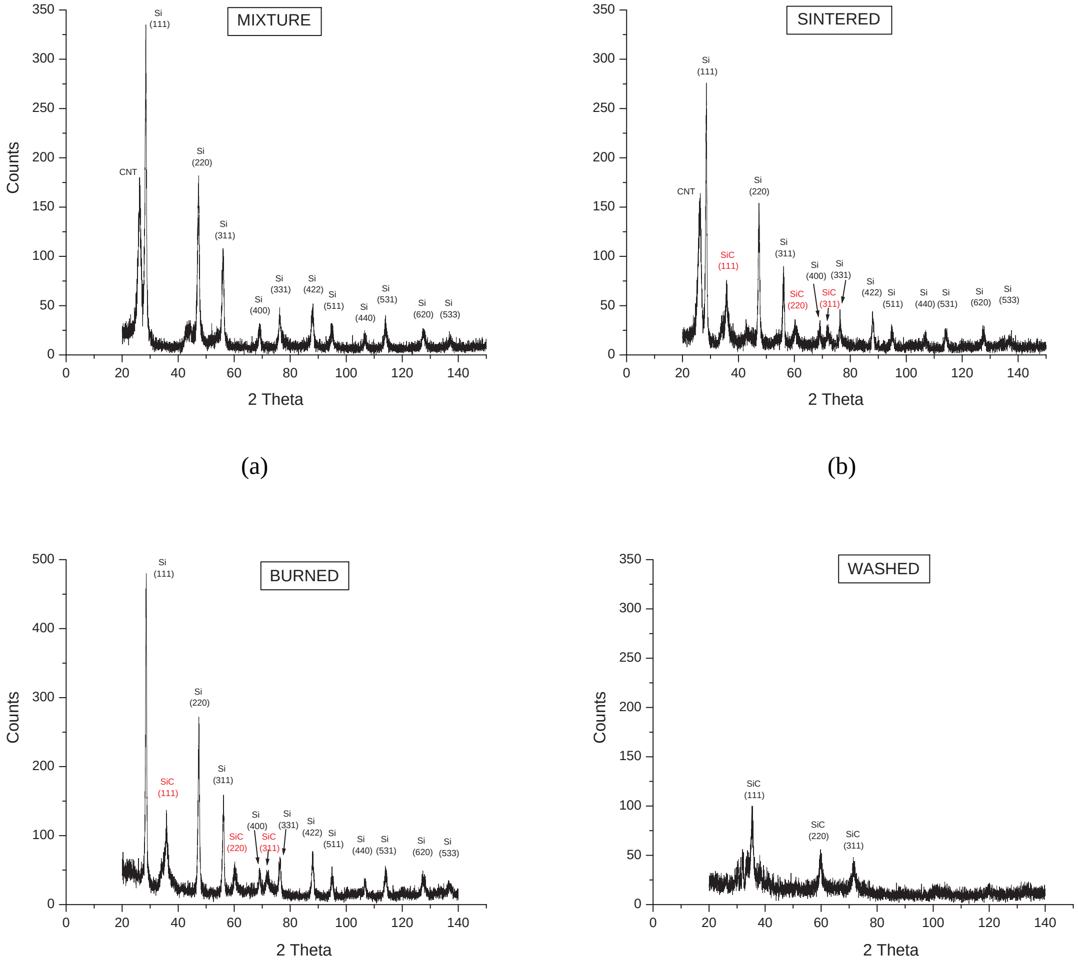

(a)

(b)

(c)

(d)

Figure 2.4: (a) Mixture of silicon nanopowder and MWNTs (3:1 molar ratio Si:C). Peak at $2\theta = 26.28$ is carbon MWNT and peak at $2\theta = 28.44$ is the [111] plane of silicon, (b) After sintering for 2 minutes in induction furnace. MWNT peak and [111] Si peak are both reduced; peak at $2\theta = 35.74$ is the [111] plane of silicon carbide, (c) After heating at 700°C for 2 hours. Peak at $2\theta = 26.28$ is gone, indicating that excess carbon was removed by burning, (d) Produced SiC after removing excess reactants. MWNT peak at $2\theta = 26.28$ and Si [111] peak at $2\theta = 28.44$ are gone. SiC [111] peak at $2\theta = 35.74$ is now dominant peak.

2.2 Experimental Methods of Characterization

2.2.1 X-ray Powder Diffraction

When x-rays were discovered in 1895, physicians and scientists began using them almost immediately as a diagnostic tool as well as to study the internal structure of dense objects. In 1912, it was found that x-ray diffraction in crystalline materials could be used to study the lattice structure of matter. Since that time, basic x-ray diffraction (XRD) has been used in essentially the same way to study many materials for a wide variety of uses, as well as to identify new materials and confirm results found by other methods. XRD can be used to identify the composition of materials as well as to determine crystal size, purity, texture, defects, and strain.

The x-rays are produced in an x-ray tube or synchrotron. A beam of x-rays is directed at the sample where the very short wavelength photons interact with electrons near the surface of the sample. The diffracted beam is detected by a photographic plate or CCD and the results are recorded. The current diffractometer usually has a goniometer so that the angle of the incident beam varies in time and the resulting diffracted beam is detected over a range of angles.

Diffraction in the crystal is described by Bragg's law:

$$n\lambda = 2dsin\theta \tag{2.1}$$

where λ is the wavelength of the diffracted light (in this case x-rays), n is the order of the bright fringe indicating constructive interference, and $dsin\theta$ is the difference in path length between adjacent diffracted rays. When the path difference between two diffracted rays is a whole number of wavelengths, constructive interference is observed and the deflected beams reinforce one another, giving a strong enough signal to be shown as a peak in the diffractogram. As the incident beam is directed along different paths, only when the crystal diffracts such that the diffracted beams from each lattice plane are in phase, producing constructive interference, will a peak be observed. Thus the peaks in the diffractogram are unique to the particular crystal structure of the sample. The angle between the incident beam and the diffracted beam is 2θ, which is the angle measured experimentally.[11]

Many patterns have been observed and catalogued so that generally, the peaks in any diffractogram can be matched with previously identified elements and compounds and their structures. As stated above, identification of composition and structure is only one use of x-ray diffraction. In addition, diffraction peaks are affected in width and shape by crystal defects of various types. Small grain size results in broadening of XRD peaks as does the presence of strain. Vacancies, dislocations, and stacking faults also have an effect on peak width and peak shape.

The x-ray diffractogram contains all the information about a sample's structure, crystallinity, size, strain, and more. Thus line profile analysis can be done in many different ways, depending on the information sought.[12] Since one of the main objectives of these experiments was to produce large quantities of high purity silicon carbide nanowires, the x-ray diffractograms have been studied to determine the composition, crystal structure and nanowire diameter, as well as the reaction rate and activation energy.

In real crystals, imperfections are invariably present and these imperfections affect the x-ray diffraction patterns. The shape of the peak is altered by the presence of stacking faults. For example, the stacking faults identified by HRSEM and HRTEM (see Chapter 5) also show up as shoulders on the peak profiles of those samples. The width of a peak may be broadened if the particles are very small and by the presence of strain in the sample. Generally, the peak is fitted as a combination of a Lorentzian function and a Gaussian function, or sometimes by a convolution of the two called a Voigt profile. The Lorentzian shape is a measure of the crystallite size and its width is proportional to $1/\cos\theta$. The Gaussian shape is related to broadening caused by strain and its width is proportional to $\tan\theta$.[12]

In his Ph.D. thesis in 1918, Scherrer derived an equation by which the particle size of a crystal could be found using x-ray powder diffraction.

$$D_{Scherrer} = K\lambda/\beta\cos\theta \tag{2.2}$$

where $D_{Scherrer}$ is the size of the particle, K is a constant equal to 0.89 for cubic crystals, λ is the wavelength of the Cu K_α x-ray radiation, β is the angular width of the peak at one-half the maximum intensity, and θ is the Bragg angle of the peak.[12] The Scherrer equation provides only a rough measure of the particle size, but the crystallite size estimated by this method is about 30 nm, which is in agreement with the sizes estimated from Raman spectra. Crystallite sizes suggested by these methods applied to long wires or fibers are assumed to correspond to the distance between stacking fault layers. A complete derivation of the Scherrer equation can be found in Reference [13].

In the earliest times of using XRD in physics or materials research, crystals were measured using the method described by Laue in which a single crystal is fixed with respect to the x-ray beam. The diffracted beam represents those wavelengths for which Bragg's law is satisfied for the spacing between planes in the lattice (d) and the angle of the incident spectrum of x-ray radiation (θ). Thus for the Laue method, θ is fixed and λ is variable. The powder diffraction method used in these experiments uses monochromatic x-rays of fixed wavelength, and the angle θ is varied by use of a goniometer. The powder consists of many small crystal grains, each of which will be aligned along some plane, [111] for example. Since there are many of these small crystals in the powder, there will be many crystals at each orientation, and the diffraction by each of these small grains will add together, grouped by the plane of orientation, thus producing high intensity peaks at each angle that satisfies the Bragg condition. X-ray diffractograms were obtained on Phillips PW2773 (Japan) diffractometer and on Siemens D5000, both with copper K-α radiation, $\lambda = 1.54$Å.

2.2.2 SEM and TEM

The resolution of a light microscope is limited by the wavelength of light. In order to see materials with higher resolution, it is necessary that the incident wavelength be of the same order of magnitude as the desired resolution. As demonstrated by deBroglie, electrons have a wave nature which allows them to diffract in crystals. In addition, electrons are easily accelerated and focused by interaction with magnetic and electric fields. Thus electrons, having wavelengths much shorter than visible light that are adjustable by changing the energy of the electrons, and being easily focused onto magnifying lenses by electric and magnetic fields, are an excellent substitute for light in microscopy. When electrons in a beam interact with the electrons in materials, some of them are scattered, some are transmitted, and some are diffracted. Some shell electrons will be excited to higher states, and some electrons at higher energy levels will fall into the lower level states that open up. Taking advantage of all these electron transitions allows several different types of electron microscopy to provide images of materials on the order of a few nanometers.

Transmission Electron Microscopy (TEM) images the reciprocal lattice directly by detecting those electrons that are transmitted through the material. Scanning Electron Microscopy (SEM) is more useful to study surface structure and morphology because the images are produced by scanning the sample to detect the secondary electrons that are emitted from the surface due to the excitation of shell electrons by the electron beam. Both methods of imaging have been used in this study, including some variations such as (STEM) Scanning Tunneling Electron Microscopy, which detects the electrons that are transmitted through the sample, but they are detected by scanning in a raster fashion.

By arranging the angle of incidence relative to the crystal structure of the sample and the position of the apertures, certain conditions can be set up. Since the diffraction in the crystal is different depending on the orientation of the crystal, it is possible to obtain a relatively high contrast image, called a Bright Field image, by selecting only unscattered electrons. Conversely, an arrangement allowing the deflected electrons to pass through the centered aperture produces a Dark Field image. In addition, electron microscopy is quite sensitive to defects in crystals. Thus in both SEM and TEM images, crystal structure, stacking faults, surface morphology, and amorphous phases will be shown and discussed.

TEM images were obtained using transmission electron microscopes Philips EM 300 and JEOL JEM 3010 with the accelerating voltage of 100 kV and 200 kV, respectively. SEM microscope, JEOL SM-6100, was used to examine surfaces of manufactured specimens. The probe current ranged from 10^{-12} to 10^{-6} A and magnifications ranging from ×750 to ×9500 were used. High resolution images were obtained using Hitachi S-4800 FE (Field Emission) SEM, courtesy of Hitachi High Technologies in Dallas, Texas. Accelerating voltage ranged from 1 kV to 30 kV and magnifications ranging from ×4000 to ×450,000 were used in the analysis. Ultra-high resolution images using SEM were done by Bill Roth at Hitachi High Technologies in California using Hitachi S-5500 FE SEM.

2.2.3 Raman Spectroscopy

Raman spectroscopy is an experimental method based on the Raman effect, which is an observed phenomena resulting from the interaction between light and matter. Light that is scattered when shined on some material is classified as either elastic or inelastic. Elastic scattering is the light that does not change frequency in the interaction and is commonly known as Rayleigh scattering. The scattered light that has a different frequency from the incident light is a result of the Raman effect. That different frequency may be either higher or lower than the incident light. Light scattering that results in a lower frequency than the incident light is referred to as Stokes Raman scattering while the scattered light observed at higher frequency is the anti-Stokes band.[14]

The interaction of light with matter that produces the Raman effect is actually an interaction with translational and/or rotational vibrations of molecules. The Raman effect can be approximately described using several theoretical models, either classical or quantum mechanical. The simplest quantum mechanical description begins with the fact that the energy of molecular motion is quantized into discrete allowable energy states. To change the state of a molecule, a quanta of energy must be absorbed or emitted by the molecule. The energy emitted or absorbed is a multiple of a quanta of energy: $\delta E = h\nu_k$, where h is Planck's constant and ν_k is the classical frequency of the molecular motion or of one photon of electromagnetic radiation. A photon absorbed by the molecule (a photon is annihilated) and subsequently re-emitted (a photon is created) by the molecule, describes elastic scattering if the two photons are identical, leaving the molecule unchanged. If the photons are not identical, the molecule will be left in a changed state–either higher or lower energy. This interaction describes the Raman effect. If the created photon is less energetic than the incident one, the frequency of the scattered light will be lower than the frequency of the incident light–described earlier as the Stokes Raman spectra. In the other case, the anti-Stokes band results.

Spectra are usually displayed in cm^{-1}, referred to as reciprocal centimeters, scale. This is done to make the numbers displayed on the graph more reasonable, since the vibrational frequency of a molecule is typically of order 10^{12}s^{-1}. The frequency is divided by the speed of light to obtain a wavenumber in reciprocal centimeters. The Rayleigh line will appear at the same wavenumber as the incident light, since it represents elastic scattering. The anti-Stokes band will then appear to the left of the Rayleigh line, and the Stokes scattered wavenumber will be to the right. Although there are many applications appropriate for using Raman Spectroscopy, the advantage to using it in the analysis presented here is that it may be used to analyze localized volumes, in contrast for example to x-ray powder diffraction, where the constituents may be known, but not how they are distributed over the local volume. Chemical compositions, molecular configurations and conformations, morphology to a small extent, strain and defect analysis in crystals are just a few examples of how Raman microscopy is being used to characterize materials. Investigation of regions less than 1 μm has elevated Raman spectroscopy to being a useful complement to other microanalysis tools such as scanning electron microscopy, x-ray micro-analysis, transmission electron microscopy, and others.

Raman spectra were obtained using a Raman microimaging system composed of an argon ion laser operating at 514 nm wavelength, an Olympus BH2 microscope, and a transmission dispersive spectrometer from Kaiser equipped with a CCD detector. The laser power at the surface of the sample varied from 10 mW to 150 mW. Spectral resolution was 4 cm^{-1}. The objective, $\times 100$, allowed collecting scattered light from spots less than 1 μm in diameter. The spectra were obtained with exposure times of 1 minute, and were analyzed using Grams software.

FTIR spectra were obtained on a Nexus 670 produced by Thermo Nicolet. A small amount of SiC powder was mixed with potassium bromide (KBr) and pressed into pellets. Resolution was 4 cm^{-1}.

2.3 Induction Heating

An induction furnace was used in the first set of experiments to heat a mixture of silicon nanopowder and carbon multiwalled nanotubes. This section begins with an introduction to heating by induction, then continues with a discussion of the skin effect and screening of the magnetic field. The data presented in this section represent experiments that were done in order to become familiar with use of the induction furnace, the temperatures reached and the amount of time needed to reach those temperatures, and limitations imposed on the experiments for optimal use of the equipment.

The foundation for induction heating is using an induced current to produce Joule heating. Faraday's law of induction says that a changing magnetic field will induce a current in a conductor placed in the field. In Gaussian units,

$$\nabla \times \vec{E} = -\frac{1}{c}\frac{\partial \vec{B}}{\partial t} \tag{2.3}$$

The induced emf is the line integral of the electric field around the path, and by Ohm's law, current will flow in the conductor. The total induced current may be found from the current density, $\vec{J} = \sigma \vec{E}$, where σ is the conductivity of the conductor. By Lenz's law, the induced current will flow in the direction such that the induced magnetic field will oppose the change in the applied field. The induced magnetic field is given by Ampere's law,

$$\nabla \times \vec{B} = \frac{4\pi\sigma\mu}{c}\vec{E} \tag{2.4}$$

neglecting the displacement current since the induced current dominates in this case.

In a conductor with conductivity σ, the work done by the charge carriers flowing against the resistance in the conductor is converted to heat and is given by Joule's law,

$$Q = I^2 R_E t \tag{2.5}$$

where Q is the heat generated, I is the total current, R_E is the resistance of the conductor, and t is time.

2.3.1 Skin Depth and Screening Effect

Many textbooks on electrodynamics discuss eddy currents, which are induced in a semi-infinite solid conductor. Finding that the induced current falls off exponentially as a function of the depth in the conductor, the skin-effect is described with penetration depth or skin depth δ. See for example Smythe[15].

$$\delta = \sqrt{\frac{c^2}{2\pi\mu\sigma\omega}} \tag{2.6}$$

The skin depth is derived for a solid cylinder, e.g. a wire, with current flowing down the length of the wire. If, however a cylindrical shell has an induced current flowing around the shell, the semi-infinite plane from which the skin-depth is derived becomes the limit of a cylinder and the physics is different in this case. See Figure 2.5.

Consider a cylindrical coil through which an alternating current of low frequency ω flows. The magnetic field in the interior of the coil will alternate at the same frequency and be directed along the central long axis of the solenoid. Near the center of the solenoid, the magnetic field may be considered uniform.

Inside the solenoid is a conducting cylindrical shell of inner radius R and outer radius $R+d$. See Figure 2.6. In cylindrical coordinates, the external magnetic field of the solenoid $\vec{B}_O$ will alternate along the z-axis.

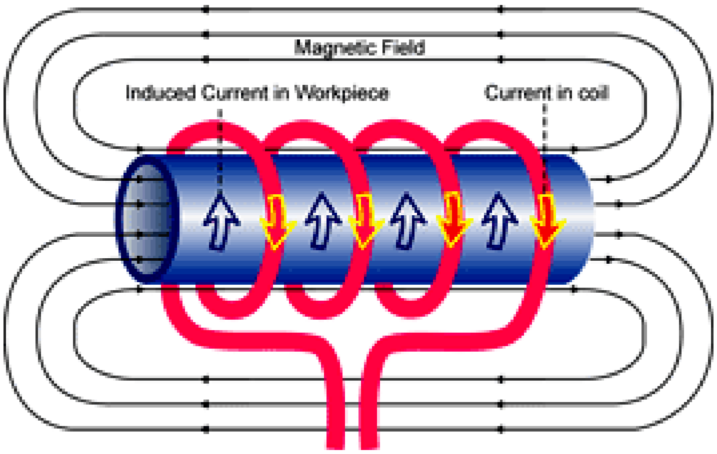

Figure 2.5: Alternating current induced in a conducting cylindrical shell inside a coil with alternating current.

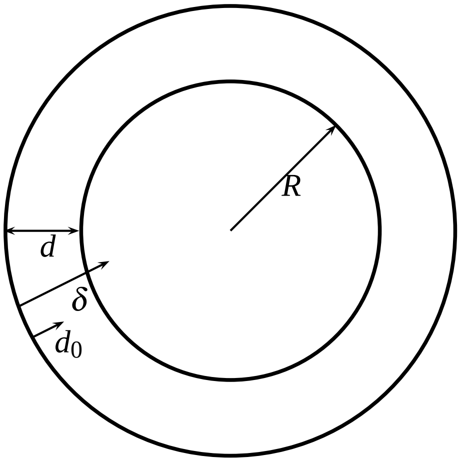

Figure 2.6: End view of cylindrical shell with inner radius R and wall thickness d. Also shown are skin depth δ and screening depth d_0.

By Faraday's law (in integral form)

$$\oint_C \vec{E} \cdot d\vec{l} = -\frac{1}{c}\frac{\partial}{\partial t}\int_S \vec{B} \cdot \hat{n} d\vec{A} \tag{2.7}$$

the changing magnetic field will induce a current flowing around the cylindrical shell such that the induced magnetic field produced by the induced current will oppose the change in the external magnetic field due to the solenoid. This induced magnetic field $\vec{B}_S$ effectively screens the inside of the shell from the external field $\vec{B}_O$. Let the resulting magnetic field inside the shell be $\vec{B}_I$ so that $\vec{B}_I = \vec{B}_O + \vec{B}_S$.[16]

The induced magnetic field inside the conductor is given by Ampere's law (Equation 2.4). The ratio of the magnetic field at the inner wall B_I to the applied field B_O, the screening factor, is [16]

$$\frac{B_I}{B_O} = \frac{1}{1 - i(\frac{Rd}{\delta^2})} \tag{2.8}$$

The screening effect behaves in the same way as the well-known skin-effect, whereby induced current flows near the surface of a conductor and falls off as a function of the shell thickness d toward the center of the cylinder. However, as shown by Fahy, et al.[16], the screening is such that the depth to which current flows inside the shell differs from the well-known skin depth δ. The inside of the cylinder is effectively screened from the applied field when $d > d_0$, where

$$d_0 = \delta^2/R \tag{2.9}$$

indicating that the screening is effective at a wall thickness much less than the skin depth.

2.3.2 Heat Generated

To find the heat generated, Q, it is necessary to find the total current inside the conductor. The frequency ω should be such that the wavelength is much larger than the conductor. In that case, the electric and magnetic fields may be considered to propagate instantaneously, which in turn justifies ignoring the displacement current in the Ampere-Maxwell law.

The time dependence is written as $e^{-i\omega t}$ and the geometry is such that $R >> \delta >> d$. From Faraday's law and the definition of current density

$$J_\theta = \frac{i\omega\sigma\mu R B_I}{2c} \tag{2.10}$$

Since the current flows around the shell, the area element perpendicular to current is $dr\,dz$. The total current is then

$$I = \int_R^{(R+d)} dr \int_0^L dz J_\theta = dLJ_\theta \tag{2.11}$$

By Joule's law (Equation 2.5), the heat generated is $I^2 R_E t$, where R_E is the electrical resistance in the conducting shell. The resistance is given by definition as $R_E = \rho L/A$. Again, since the current is flowing around the shell, the length is the circumference of the cylinder and the perpendicular cross section is dL. The heat per unit length of the cylinder is

$$Q = -\left(\frac{\omega R}{c}\right)^2 \pi\sigma\mu d t B_I^2 \tag{2.12}$$

Thus the important features of the system are the frequency of the input current to the coil, the inner radius R and wall thickness d of the cylindrical shell, and the permeability μ and conductivity σ of the conducting material from which the shell is made. And of course, the heat generated depends on the length of time during which heating occurs.

2.3.3 Induction Furnace

The output frequency, voltage, current, and power were investigated as a function of the input current setting on the power supply. These variables are measured in terms of the percentage of the maximum value reached. The unit is capable of maximum power output of 25 kW, and the frequency of the alternating current sent to the induction coil is 30 kHz.

One of the major advantages to induction heating over other methods of heating is the ability to reach a constant temperature in a known amount of time repeatedly. Since induction heating is established as a stable process, measurements of equilibrium temperatures reached at different input power should produce a reliable means of finding temperature without measuring it directly. Figure 2.7 shows a graph relating temperature to input power for a solid graphite rod.

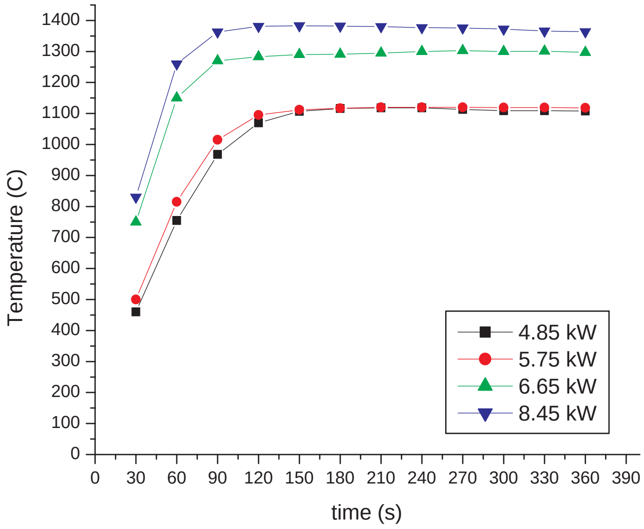

Figure 2.7: Equilibrium temperatures are reached in 2 to 3 minutes and increase as input power increases.

In each case, it takes about 2 minutes for the temperature to reach its maximum. After that time, a stable temperature is maintained as expected.

2.3.4 Crucible Material

Looking for the appropriate setting to produce a particular temperature, a graphite rod was used with a thermocouple inserted into a hole drilled in the center of the rod. It can be seen that indeed a particular temperature is reached and then held for each power setting. See Figure 2.7.

Replacing the graphite rod with a new one and repeating temperature measurements at constant input current, a noticeable change in equilibrium temperature reached occurred. Figure 2.8 shows that the equilibrium temperature dropped each time the experiment was repeated.

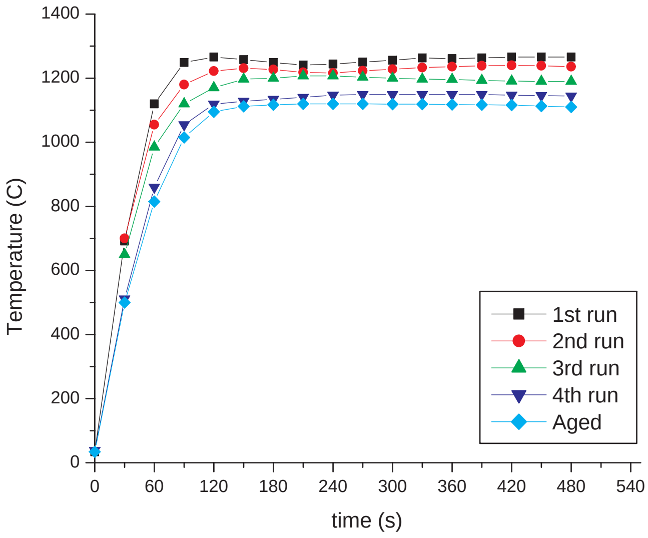

Figure 2.8: Graphite crucible aged with repeated heating such that equilibrium temperature dropped with each successive heating.

Joule heating depends on frequency, time, strength of the magnetic field (which depends on input current), permeability and resistivity of the material being heated, and radius and wall thickness of the cylindrical shell. The change in equilibrium temperature thus implies that the resistivity of the material was changing when heated, since all the other variables were held constant. Not only must there have been a change in resistivity, it must have been increasing to cause the equilibrium temperature to drop. This could have been caused by either oxidation or graphitization. To reduce oxidation, the heating was repeated in an atmosphere limiting oxygen exposure.

2.3.5 Atmosphere

After finding that the equilibrium temperature reached was not reliably consistent for a particular input setting, the exposure to oxygen was limited by first placing the graphite in argon for 1 hour to eliminate any oxygen in and around the graphite. Then the rod was heated in an atmosphere of nitrogen gas created by surrounding the coil with a container holding liquid nitrogen. Liquid nitrogen was continuously added during heating to provide an oxygen-free atmosphere throughout the period of heating.

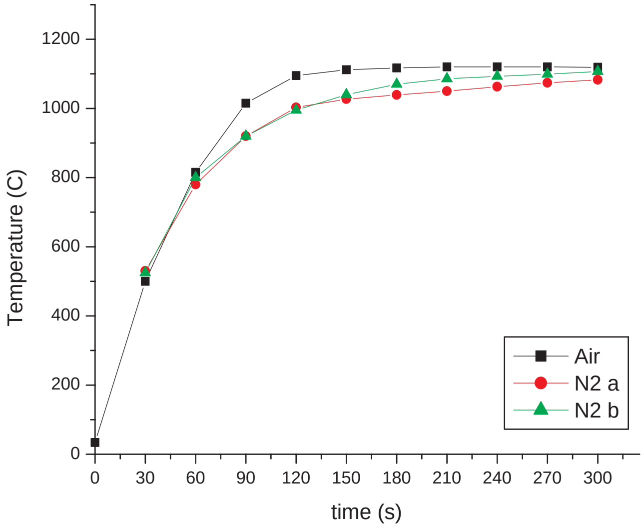

Figure 2.9: Using a nitrogen gas atmosphere reduced the change in equilibrium temperature, but also slowed the rate of heating.

Figure 2.9 shows that the temperature was indeed more stable in the nitrogen atmosphere. However, the equilibrium temperature was still changing slightly as the rod aged. Graphitization might still have been changing the resistivity, or the crudity of the method for limiting oxygen may have allowed continued oxidation. All subsequent heating experiments were done in vacuum.

To eliminate graphitization, the crucible material was first changed to stainless steel. Several experiments with a stainless steel crucible demonstrated repeatability and reliability. Oxygen was also limited in these measurements by heating in a nitrogen atmosphere, as described previously. Figure 2.10 shows that equilibrium temperature increased with increasing input power for the stainless steel crucible. The conclusion is that stainless steel is better than graphite for the crucible.

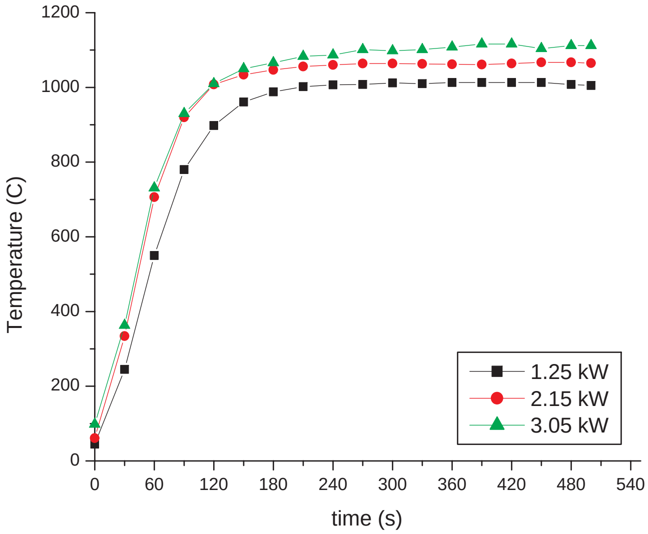

Figure 2.10: Equilibrium temperatures for stainless steel heated in nitrogen atmosphere show the expected increase in temperature with increased power input.

For the low temperature experiments done with the induction furnace samples, the crucible used was made of stainless steel and a nitrogen atmosphere was maintained during heating. However, stainless steel melts at 1420°C, which made it unsuitable for the higher temperature sintering. After the method was demonstrated to work adequately, the set-up was improved to allow the sample to be held under vacuum conditions, and the crucible material was changed to tantalum, melting temperature 2996°C, which proved to be a more suitable crucible material for the remaining measurements to find the reaction rate.

2.3.6 Crucible Radius and Wall Thickness

Three stainless steel crucibles, each having different inner radius R and/or wall thickness d, were heated at the same power setting in a nitrogen atmosphere. The first was labeled STn for small radius, thin wall. The second one, LTk, had a larger radius and thicker wall. STk had the same small radius as STn, but a much thicker wall. Since resistance heating Q is proportional to wall thickness d and to the square of inner radius R^2 as given by Equation 2.12, it was expected that LTk would be the easiest to heat and would reach the highest temperature. Table 2.3 describes the 3 crucibles and shows the temperature $T\,(^\circ C)$ reached for each crucible, conductivity $\sigma(s^{-1})$ (depends on temperature), skin depth δ (mm), and screening depth d_0 (mm), along with comparisons of the last two parameters with R and d. Resistive heat Q was calculated in terms of constant values comprising Q_0, where $Q = \sigma R^2 d Q_0$. (Compare to Eq. 2.12).

Name	T $(^\circ C)$	σ $(10^{15}s^{-1})$	R (mm)	d (mm)	δ (mm)	d_0 (mm)	R/d_0	d/δ	d/d_0	Q (Q_0)
STn	1040	6.60	5.84	0.51	3.47	2.06	2.8	0.1	0.2	12.8
LTk	1145	6.31	6.80	2.73	3.55	1.85	3.7	0.8	1.5	88.5
STk	1335	5.83	5.84	3.12	3.69	2.33	2.5	0.8	1.3	69.0

Table 2.3: Crucibles STn, LTk, and STk as described in the text. R is inner radius, d is wall thickness, δ is skin depth and d_0 is the wall thickness parameter for the screening effect. Q is the heat generated according to Eq. 2.12 in terms of Q_0, where $Q = -R^2\sigma d Q_0$.

Table 2.3 shows that the resistive heat Q was higher for LTk. The third crucible STk (small R, large d) did not follow the trend. The calculated value of Q indicates that its equilibrium temperature should have fallen between the temperatures of STn and LTk, but instead a higher temperature was reached. More experiments might explain this anomaly, but here the focus remained on the trend confirmed by STn (small radius, thin wall) and LTk (large radius, thick wall). The ratios given show that the skin depth was not relevant for these crucibles since d/δ was less than 1 for each one. Because the skin depth was always deeper than the wall thickness, then the field was sufficiently constant throughout the crucible. The ratio R/d_0 shows that the radius was about 3 times the screening depth, and the wall thickness was the same order of magnitude as the screening depth as given by the ratio d/d_0; both ratios indicate that the inside of the crucible was not screened from the eddy currents at the surface.

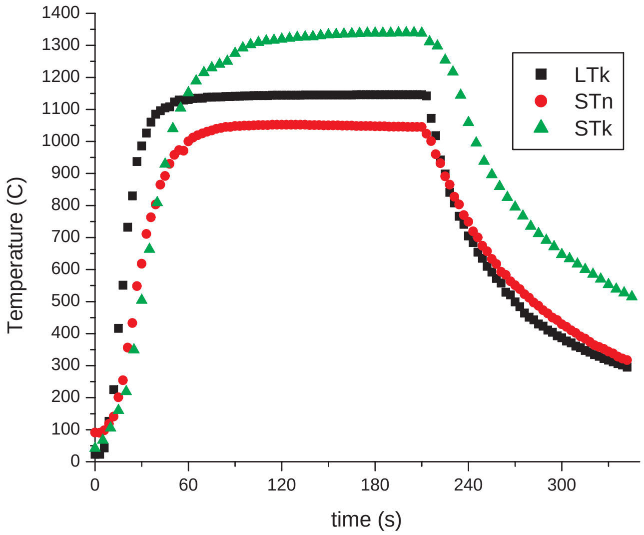

Figure 2.11: The large diameter crucible with a thick wall (LTk) heated fastest and reached a higher temperature than the ones with smaller radius. The lowest temperature reached was by the crucible with smaller diameter and the thinner wall, which was expected. The highest curve was the small radius thick wall and did not agree with predictions; however, more experiments would have been needed to follow-up on this anomaly.

In Figure 2.11, a comparison of STn (small radius, thin wall) to LTk (large radius, thick wall), confirmed the expected trend. LTk (large R and d) not only reached a higher equilibrium temperature, but it also heated and cooled more quickly. A higher rate of heating and cooling is desirable, since it reduces the error in measurement of reaction time. See Chapter 3 for more details on reaction time.

The skin effect refers to the fact that current passing through a solid conductor is generally confined to a depth very close to the surface. This depth, called the skin depth δ, is the distance from the surface through which the wave amplitude decreases by a factor of $1/e$. Equation 2.6 shows that the skin depth depends on three variables: the frequency ω of the alternating current, which is constant for the induction furnace; the permeability μ of the conductor, which is constant for a given material ($\mu = 1.008$ for stainless steel); and the conductivity σ of the conductor, which is inversely proportional to temperature. In this case, the skin depth for each crucible depends on the conductivity at the temperature reached, so each has been calculated and included in Table 2.3.

In addition, the thickness at which screening of the applied magnetic field becomes relevant is of interest. See Section 2.3.1 for a description of screening. The screening depth d_0 depends on δ and has been calculated for each crucible. Comparing the actual wall thickness d to both the skin depth δ and the screening depth d_0 shows that neither of these phenomena played a role here. The increased resistivity of the stainless steel, due to the high temperatures reached in these experiments gives δ larger than d, and $d_0/d > 0.5$ in all cases. Thus, although heating increases with radius and wall thickness, the skin effect did not occur in the crucible wall, and any slight screening of the interior from the applied magnetic field did not have much, if any, effect on heating. This result is reasonable since the skin effect only applies when $\delta \ll R$ and screening is only effective for $d \ll \delta \ll R$.

2.3.7 Temperature

For the induction furnace experiments, it was unnecessary to measure temperature in general, since one advantage of induction heating is the stability of the temperature. After running initial experiments correlating temperature reached with input power selected on the power supply, some experiments were done without measuring temperature by any other method. However, once the procedure was established with crucibles made of appropriate material for the temperature being measured and vacuum established as constant, most experiments were done with a thermocouple inserted into the sample. Using the thermocouple allowed better tracking of heating and cooling, and ensured that samples were held at constant temperature for the selected reaction time.

Figure 2.12 shows that in general, the higher the temperature reached, the faster the heating and cooling. In another set of experiments, the minimum reaction temperature was found to be 1000°C. Below this temperature, no SiC product was formed.

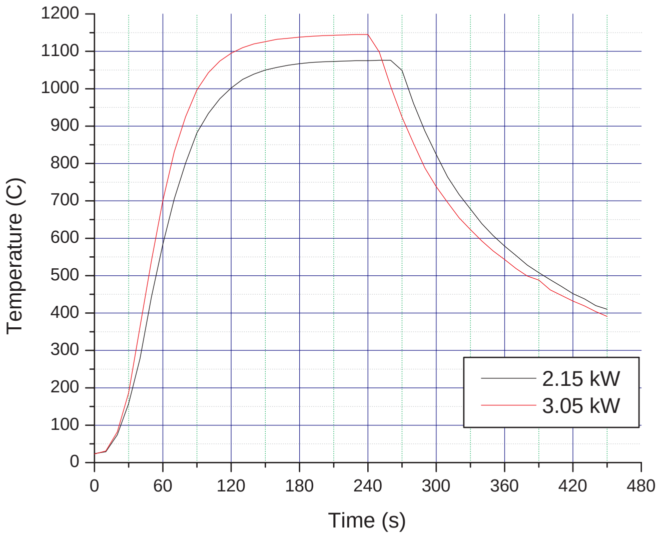

Figure 2.12: Temperature as measured in degrees Celsius shows how quickly samples heat and cool by induction and how increased input power increases the maximum temperature reached.

The maximum temperature reached for input power 2.15 kW was 1075°C and for 3.05 kW, 1145°C. Different rates of heating and cooling were also observed in the comparison data of crucible radius and wall thickness, Figure 2.11. The pattern exhibited by LTk (crucible with large radius and thick wall), in which heating and cooling were faster, is preferred in order to minimize the error in reaction time by reducing the time to reach the desired temperature after having reached the minimum reaction temperature. Heating and cooling are also affected by the material from which the crucible is made.

Chapter 3

Reaction Kinetics

3.1 Reaction Kinetics in Solids

The primary purpose of a kinetics study is to determine the reaction mechanism(s) involved in a particular chemical reaction. Because all particles do not have sufficient energy for transformation, only a fraction of the particles participate in the reaction at any given time. There may be several different possibilities for the mechanism of reaction, and each path is associated with a free energy curve. The activation energy is related to the reaction path taken in a particular reaction.[17]

In general, the reaction mechanism is determined by measuring the reaction rate at different temperatures then fitting the plot to various theoretical functions that have been determined from a model of the reaction based on the geometry of the interface, initiation methods, and advance and/or diffusion processes. Chemical kinetics has been studied since the late 19th century, but only recently have technological advances in detection techniques allowed serious kinetics studies of solid-solid reactions. The literature in this field is thus limited to studies beginning within the last 50 years or so.

Most solid-state chemical reactions are accomplished in two or three steps. The product forms between the reactants, so one reactant must pass through the product to the second reactant in order for the reaction to continue. In time, the product layer grows and diffusion through that layer takes longer. In general, the first step involves transport of one reactant to the interface, and the second step is the chemical reaction. A third possible step may involve diffusion of the product into the growing phase.[18] The reaction kinetics of any solid state reaction may be affected by any or all of the following parameters[19]:

1. Reactants - identities, compositions, relative quantities
2. Particle Sizes - size, shape, size distributions
3. Mixing - relative dispositions of components, method of mixing, pretreatment
4. Products - identification of all products
5. Yield-time Data - measurement of changes in time of amounts of reactants and product
6. Temperature - effects on above parameters.

The rate of reaction, is the rate at which the concentration of each reactant and the product changes. Consider a chemical reaction:

$$aA + bB \rightarrow cAB \tag{3.1}$$

The rate of reaction may be expressed as the rate of increase of the product (+), or as the rate of decrease of either reactant (-).

$$k = \frac{1}{c}\frac{d[AB]}{dt} \tag{3.2}$$

In the case of a solid-solid reaction where the reaction takes place at the interface, the reaction may be controlled by nucleation or diffusion. Hulbert[20] has provided an analysis of rate laws for appropriate models of diffusion-controlled growth processes.

The general expression is of the form

$$-\ln(1-\alpha) = (kt)^n \tag{3.3}$$

where α is the fractional remains of the reactant on the interface and k is the rate constant of the chemical reaction, which is independent of concentration and time, but increases rapidly with increasing temperature. The exponent $n = (\beta + \lambda)$ is used for interface-limited reaction models and $n = (\beta + \frac{\lambda}{2})$ is used for diffusion-controlled reactions. In Hulbert's analysis, the possibilities under consideration are that nucleation is (i) instantaneous ($\beta = 0$), (ii) constant ($\beta = 1$), and (iii) deceleratory ($0 < \beta < 1$) for nuclei growth in one, two, or three dimensions ($\lambda = 1, 2,$ or 3), respectively. Table 3.1 shows expected values of the parameter n for these models in one, two, and three dimensions.

Model		Parameter (n)
Three-dimensional growth (Spherical particles of reactant) Nucleation rate	(1) Constant	2.5
	(2) Zero (instantaneous)	1.5
	(3) Deceleratory	1.5 - 2.5
Two-dimensional growth (Laminar particles of reactant) Nucleation rate	(1) Constant	2.0
	(2) Zero (instantaneous)	1.0
	(3) Deceleratory	1.0 - 2.0
One-dimensional growth (Lath-shaped particles of reactant) Nucleation rate	(1) Constant	1.5
	(2) Zero (instantaneous)	0.5
	(3) Deceleratory	0.5 - 1.5

Table 3.1: Expected values of n for interface-limited reaction models and diffusion-controlled reactions in one, two, and three dimensions, where the reaction rate law is given in Equation 3.3[20]

The well-known Arrhenius Equation (Equation 3.4), postulated in 1897, explains why the same molecules will react at different rates in different chemical reactions. Arrhenius explained that in order for a molecule to react, it must possess a minimum critical energy known as the activation energy. Experiments continue to verify this postulate, which also shows how the rate constant k varies with temperature T:

$$k = A \exp\left[-E/(RT)\right] \tag{3.4}$$

where E_a is the activation energy, R is the molar gas constant, and A is an integration constant.

The activation energy is then the energy required by a system to initiate a particular process. For most reactions, the activation energy is found (experimentally) to be temperature independent. To determine the activation energy for a particular reaction, a plot of natural log of the reaction constant vs. reciprocal temperature is made, and the activation energy is calculated from the slope of the line.[21]

Solid-solid reactions of the type given in Equation 3.1, have been studied to determine the rate processes involved. Characteristic of these reactions is the formation of a barrier phase of product at the interface between reactants. As the reaction proceeds, the barrier grows in thickness and thus always affects the reaction rate in these systems. One or both of the reactants must diffuse through the product phase to reach the other reactant in order for the reaction to continue. The diffusion rate for the reactants is controlled by the size of the product barrier, as well as the temperature and pressure maintained during the reaction.

3.2 Measurement of Rate Constant k

The reaction rate for nanostructured silicon carbide has been studied for all the samples heated by induction and for one temperature of the vapor phase experiments. In the induction experiments, a mixture of reactants was heated quickly by induction. Multiple measurements were made at nine different temperatures, varying heating time from a few seconds up to several minutes, see Table 3.2.

From the x-ray diffractogram measurements, the reaction rate and activation energy were determined for the mixture of solid reactants. The tube furnace experiments were done with the

Temperature (°C)	Time (s) (unless otherwise noted)	SiC Concentration Mass SiC(Mass Si + Mass SiC)
1040	150 – 900	0.017 – 0.079
1100	120 – 900	0.036 – 0.18
1175	30 – 900	0.054 – 0.25
1250	60 – 1800	0.072 – 0.39
1325	30 – 900	0.086 – 0.53
1450	13 – 480	0.38 – 1.0
1490	8 – 360	0.087 – 1.0
1510	70 – 240	0.69 – 1.0
1550	13 – 360	0.78 – 1.0
1200	1hr - 8hr	.017 – 0.94

Table 3.2: SiC concentration found for multiple reaction times at each temperature. The SiC concentration shown here in the last row is [Mass SiC / (Mass C + Mass SiC)] since the unreacted silicon in the vapor phase experiments remained in the quartz tube, separated from the MWNTs and SiC.

reactants separated and heated to the sublimation temperature of silicon in a resistance furnace, providing information for studying the reaction rate and activation energy for the vapor phase reaction of silicon with solid MWNTs.

Table 3.2 shows the temperatures used in these experiments, the range of times for each temperature, and the range of SiC concentrations produced. All but the last temperature represent samples heated by induction, with temperatures from 1040°C to 1325°C producing SiC from solid reactants and temperatures 1450°C to 1550°C producing SiC from liquid silicon. The last temperature in Table 3.2, 1200°C, is the tube furnace experiments, where SiC was produced from silicon in the vapor phase and carbon, both solid and vapor. The resulting morphology and structures produced by these last experiments have been carefully analyzed and are reported in Chapters 4 and 5, respectively.

The induction furnace is equipped with a timed mode, which allows the user to set a specific time of heating after which the current automatically shuts off. In order to track trends in heating and determine errors in timing, periodic temperature readings (every 5 seconds, 10 seconds, etc.) were taken. As mentioned in Chapter 2, early experiments showed that no reaction occurred by the induction method at temperatures lower than 1000°C.

Reaction time is measured as the time during which the temperature is held at a constant value (within 10% in these experiments). However, the reaction may have actually started as soon as the temperature reached the minimum reaction temperature, in this case 1000°C. Thus the error in the measured time and the actual time during which the reaction may have occurred is greatly reduced by heating and cooling very quickly, which is made possible by heating in an induction furnace.

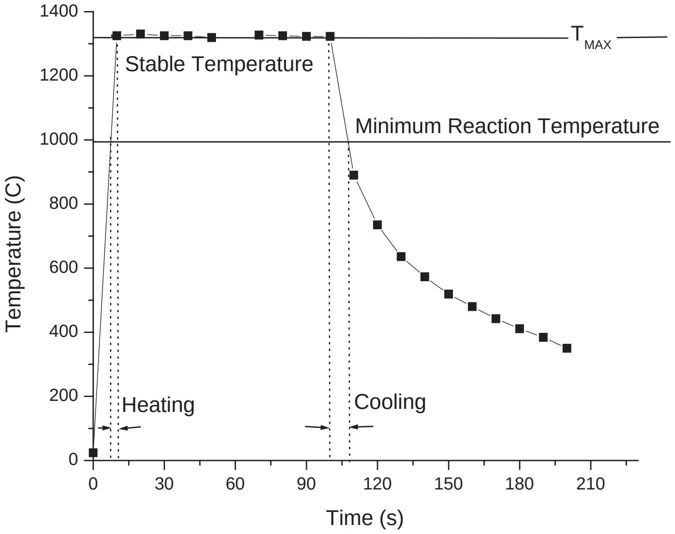

Figure 3.1: Temperature readings taken every 5 seconds provided accurate information for the error in measured reaction time.

In general, the higher the temperature reached, the faster the heating and cooling. (See Figure 2.12 in Chapter 2.) Measurement of the reaction time was more precise than for the tube furnace samples, but because of gradual heating and then cooling of the samples, there was still significant error in determining the reaction time especially for short times and high temperatures.

To improve determination of the reaction time, the temperature at which SiC formation starts (1000°C) was used as the starting point. In Figure 3.1, this temperature is marked with a horizontal line labeled as the Minimum Reaction Temperature. This minimum reaction temperature was found to be in agreement with the observation by Teo and Sun[22] that SiC starts forming at T > 1025°C. The reaction time was determined as the stable temperature time plus half of the heating and cooling time above the minimum reaction temperature, 1000°C. The precision of reaction time determined in this way is half of the heating and cooling temperature. The relative error is higher either for shorter times or for higher temperatures.

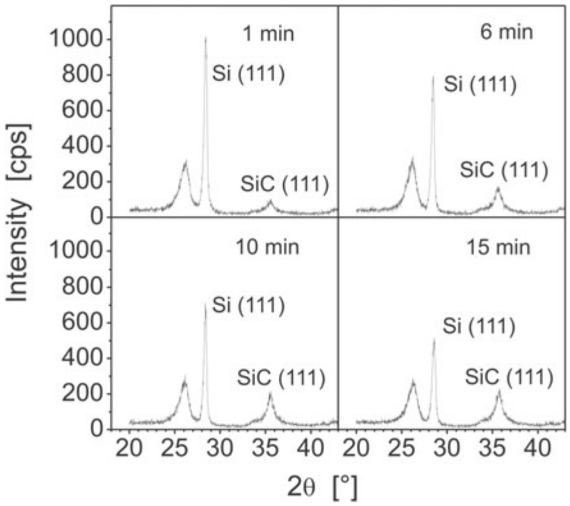

Figure 3.2: Comparison of SiC [111] and Si [111] peak intensity as reaction time increased from 1 minute to 15 minutes.

At least 5 and up to 15 measurements were made for each temperature. The SiC mass concentration was determined from comparison of the x-ray peak intensities. Figure 3.2 shows how the SiC [111] peak ($2\theta \approx 35°$) increased while the Si [111] peak ($2\theta \approx 28.5°$) decreased as reaction time increased. The relationship of peak intensity concentration to mass concentration was determined experimentally for both methods of production. The SiC mass concentration was then plotted against time, and a two-parameter fit to the Arrhenius equation was done in order to find the rate constant k (and the parameter n) for each temperature.

For the vapor phase experiments, any unreacted silicon powder remained separated from the unreacted carbon and produced silicon carbide. In this case, the concentration of SiC was found by comparison of SiC peak intensity to the MWNT peak intensity. The relationship between peak intensity and mass concentration was again found experimentally and the concentration used in the two-parameter data fit to the Arrhenius equation, just as was done in the induction experiments. With the conventional oven, heating took much longer, of course, so the reaction time was measured from the time operating temperature (1200°C) was reached, again within 10%, to the time the temperature fell below the minimum reaction temperature, which was much lower in the resistance furnace, 850°C.

3.3 Experimental Results

To determine the reaction rate for the mixture of silicon nanopowder and carbon multi-walled nanotubes heated by induction to form nanostructured silicon carbide (the induction furnace samples), x-ray diffraction peaks were measured and compared. The relationship between peak intensity and mass concentration can be found experimentally by measuring peak intensity for several known concentrations of silicon carbide and silicon. Pantea made such measurements and found the following relationship[23]:

$$y = 0.36x^2 + 0.64x \tag{3.5}$$

where y is the mass concentration of silicon carbide to remaining silicon and silicon carbide, and x is the x-ray diffraction peak ratio of silicon carbide to remaining silicon and silicon carbide. One measurement of known concentration was confirmed to lie on the curve found by Pantea (within 10%), see Figure 3.3.

Each induction furnace sample was examined by XRD, which was used to determine the concentration of SiC. X-ray diffractograms were obtained on Phillips PW2773 diffractometer described in Chapter 2. By this method, x-ray diffraction peaks of Si [111] peaks and SiC [111] were fitted using a Voigt profile,[24] and the intensities of fitted peaks were used to determine SiC mass concentration for each reaction time at each of the nine different temperatures.

Determination of the reaction rate is the first step in understanding the reaction mechanism. Recall the rate law for solid-solid reactions has a general form given by Equation 3.3. In order

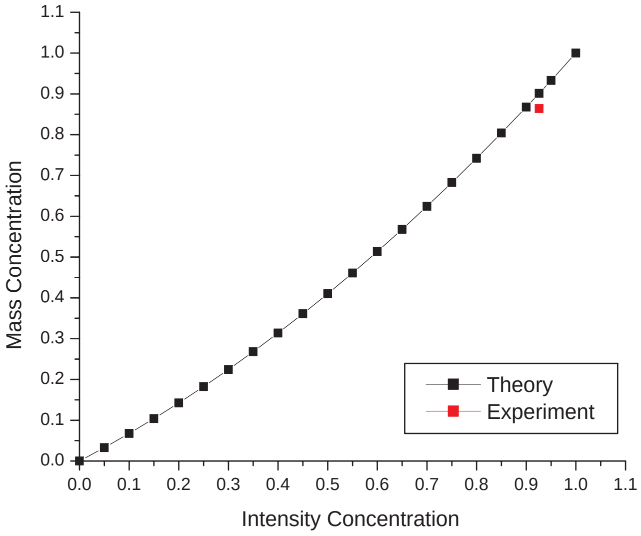

Figure 3.3: Theoretical curve from Equation 3.5 shows the relationship between mass concentration and peak intensity of x-ray diffraction data.

to find the rate constant k and the exponent parameter n, data for SiC concentration and time of reaction were accumulated and plotted as shown in Figure 3.4. A two-parameter fit to the equation then provided values of k and n for each specific temperature. The results of the two-parameter data fitting to the Avrami-Erofeev model[25]–[26],[27] to find the reaction rate constant k and parameter n for all temperatures are shown in Table 3.3.

T(°C)	$k(10^{-5})$	n
1040 ± 10	8 ± 4	0.8 ± 0.9
1100 ± 10	35 ± 24	0.69 ± 0.21
1175 ± 10	25 ± 15	0.64 ± 0.15
1250 ± 10	27 ± 2	0.45 ± 0.02
1325 ± 10	218 ± 17	0.52 ± 0.04
1450 ± 10	879 ± 3	1.58 ± 0.03
1490 ± 10	5500 ± 1600	1.08 ± 0.21
1510 ± 10	1100 ± 4200	2 ± 20
1550 ± 10	3380 ± 240	1.16 ± 0.13

Table 3.3: Results of two-parameter data fitting to Avrami-Erofeev law to find the reaction rate constant k and parameter n for all temperatures.

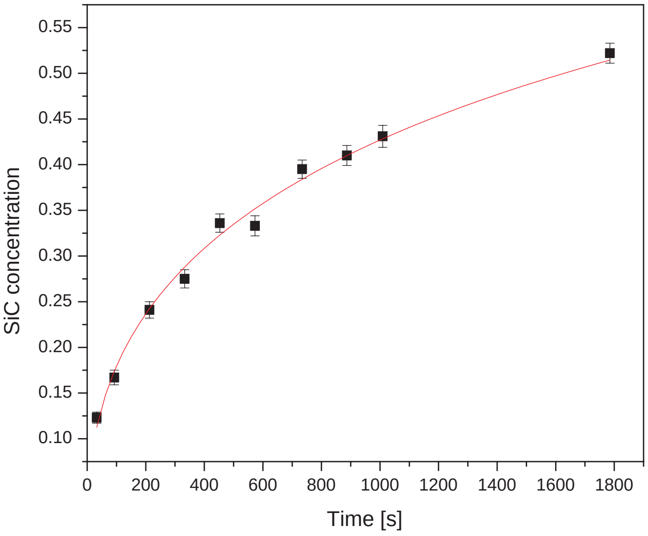

Figure 3.4: Calculated SiC mass concentration vs. reaction time for 1250°C. Data are fit to the general reaction rate law from the Avrami-Erofeev model.

3.3.1 One- and Two-dimensional Growth

Results for the value of n given in Table 3.3 show that the reaction mechanism was probably diffusion-controlled one-dimensional growth with a decelerating nucleation rate up to the temperature 1325°C. The significant change in the value of n starting from 1450°C leads to the conclusion that, beginning at this temperature, 2-dimensional growth was observed. In fact, at higher temperatures, individual nanowires fused together to form planar structures as confirmed by SEM and TEM images, see Chapter 4.

3.4 Activation Energy

The mechanism of nanosize SiC formation has not been fully characterized. The high-temperature interaction in the silicon-graphite system has been investigated by Gorovenko, et al.[28]. The process was a liquid-phase reaction, and the activation energy was determined to be 220 kJ/mol. In previous research, Pantea, et al.,[29] studied SiC formation from the precursors diamond and silicon under high-pressure high-temperature conditions. Activation energies were found ranging from 170 kJ/mol for nano-diamond to 260 kJ/mol for micro-diamond. The value of the activation energy for the induction furnace samples in this study, (254 ± 36) kJ/mol, is in good agreement with those obtained by Pantea, et. al.[23],[29] for the diamond-silicon reaction.

Table 3.4 shows values of $\ln k$ vs. T^{-1} plotted, along with error values for the rate constant k for the induction furnace samples. High error values for 1510°C are due to the very small number (only three) of measured samples.

Once values of the reaction rate constant k were found for each temperature, the activation energy E_a was found from the Arrhenius equation (Equation 3.4) by plotting $\ln k$ vs. T^{-1} as shown in Figure EaPlot. The slope of the best fit line of the data in Figure EaPlot was used to calculate the activation energy, which was found to be (254 ± 36) kJ/mol.

In this study, the induction furnace samples were used to obtain the activation energy of the reaction between silicon nanopowder and MWNTs. Previous results by Wang, et al.[3]

T(°C)	T(K)	$1/T(1/\text{K})$	k	k-error	$\ln k$
1040	1313	7.616×10^{-4}	3.0×10^{-5}	1.0×10^{-5}	-10.4
1100	1373	7.283×10^{-4}	7.0×10^{-5}	6.0×10^{-5}	-9.6
1175	1448	6.906×10^{-4}	2.7×10^{-4}	8.0×10^{-5}	-8.2
1250	1523	6.566×10^{-4}	1.0×10^{-4}	2.0×10^{-5}	-9.2
1325	1598	6.258×10^{-4}	2.7×10^{-4}	2.2×10^{-4}	-8.2
1450	1723	5.804×10^{-4}	6.5×10^{-3}	2.0×10^{-5}	-5.0
1490	1763	5.672×10^{-4}	4.2×10^{-2}	1.5×10^{-2}	-3.2
1510	1783	5.609×10^{-4}	4.0×10^{-2}	8.0×10^{-2}	-3.2
1550	1823	5.485×10^{-4}	2.4×10^{-2}	2.0×10^{-4}	-3.7

Table 3.4: Temperatures are given in Celsius, converted to Kelvin, then the inverse is given, values of k are given with errors, then $\ln k$. Plot of $\ln k$ vs. T^{-1} was used to find the value of the activation energy for the reaction.

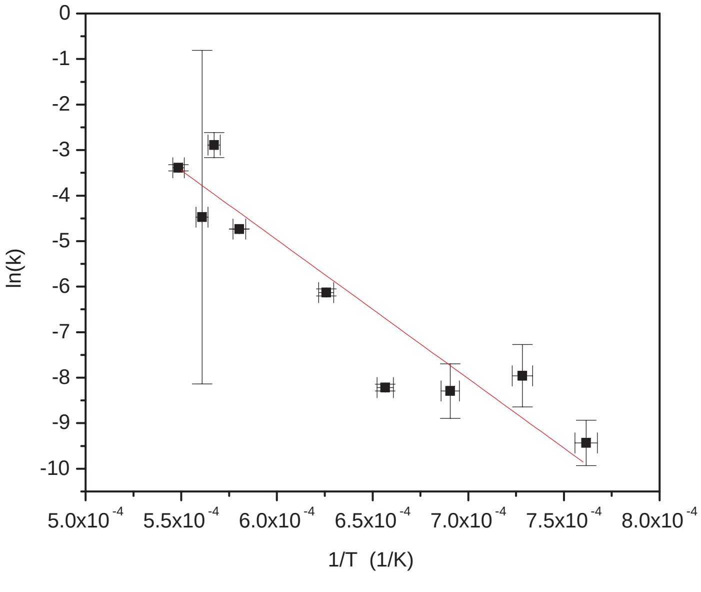

Figure 3.5: Data fitting of Arrhenius equation (Equation 3.4). Very high error value for one point is connected to a small number of fitted points. The straight, dashed line is a result of linear fitting where R is the molar gas constant, and E_a is the activation energy.

sintering SiC nanowires from the same precursors under high pressure (2 GPa) showed the activation energy was (96 ± 29) kJ/mol. The activation energy obtained there was the result of a 3-point fitting, for a narrow range of temperatures, which is not comparable with the results obtained from the wide range of temperatures used in this study, especially if the mechanism was changing with temperature. The fitting made using only the 3 lowest temperatures in this experiment resulted in a value of activation energy much lower than that obtained using all temperatures. Also, the results obtained by Pantea show the tendency of the experiments sintered under higher pressure to diminish the value of the activation energy. The tendency can be attributed to the changing volume of the reaction, which is smaller for higher pressures. The values found here for k and n are in agreement with those results. The reduced energy of activation observed for the reaction run under high pressure conditions indicates that the limiting factor is the diffusion of atoms through the SiC product layer. Increased pressure increases the population of defects and enlarges the volume of grain boundaries thus enabling faster diffusion of atoms.

Chapter 4

Morphology

4.1 Growth of SiC Nanowires

Currently, the growth of nanostructured materials is poorly understood. Although the enhanced physical and mechanical properties of these materials are widely known, the mechanisms that produce the enhancements are still a mystery. The morphology and structure of the SiC nanowires produced for this study definitely changed with increased sintering time. Analysis of the progression of these morphological changes suggests that different reaction phases mediated growth and produced different structures and features. Comparing the morphology of nanowires produced by sintering for different times has identified several types of growth as well as a timeline for each stage. Regardless of how growth was mediated, the entire reaction was diffusion-controlled.

In order to describe morphological changes that occurred in time, SiC nanowires were produced by vaporization of silicon, starting with the same precursors each time, evacuating the ampoule containing the separated reactants the same way, and sintering in the same furnace under the same conditions, so that the only variable was time. Starting with 1 hour, samples were sintered for 2 hours, 3 hours, 4 hours, 6 hours, and 8 hours at 1200°C in a tube furnace. In addition, one sample was sintered for 64 hours in a conventional furnace, and two samples were produced from aligned multiwalled nanotubes. Those 2 samples were sintered for 20 hours and 26 hours. All samples consisted of a molar ratio of 2 micro Si: 1 C except Sample CFA64, for which the molar ratio was 3 nano Si: 1 C. See Table 2.1 in Chapter 2 for the complete description of all tube furnace samples.

Initial studies indicated that sintering times less than 1 hour did produce SiC, but in quantities insufficient for meaningful analysis. The reaction run for 64 hours showed that all carbon nanotubes completely reacted so longer runs were unnecessary. By keeping the silicon separated and interacting only in the vapor phase, this method successfully produced SiC nanotubes and nanowires, with no other structures. Although unreacted carbon remained in most samples, burning in air successfully removed the carbon so that the study was done on high purity SiC nanotubes and SiC nanowires.

For the comparison presented here, only selected samples are shown, all of which are representative of the changes observed and the times for which significant changes in morphology were characteristic. The chosen samples were sintered for 1 hour, 3 hours, 6 hours, 8 hours, 20 hours, and 64 hours. The structure of the produced material has been analyzed by several different methods. In this chapter, SEM and TEM images are presented and discussed along with high resolution SEM (HRSEM) and TEM (HRTEM) images. X-ray powder diffraction profiles, Raman spectra and FTIR spectra are also discussed.

4.2 Initial Observations

The crystal structure of carbon nanotubes is a rolled graphene sheet, i.e., a collection of hexagonal rings of carbon atoms forming each layer (one layer being a single-walled nanotube), with ends that are hemispheres of the fullerene structure of carbon.

Figure 4.1 (SEM) shows the smooth curls of the precursor carbon MWNT (tangled). In general, the MWNTs are seen to be fairly uniform in diameter, having outer diameters ranging from 60 to 100 nm and lengths between 5 and 15 μm. In the image shown, the MWNTs appear

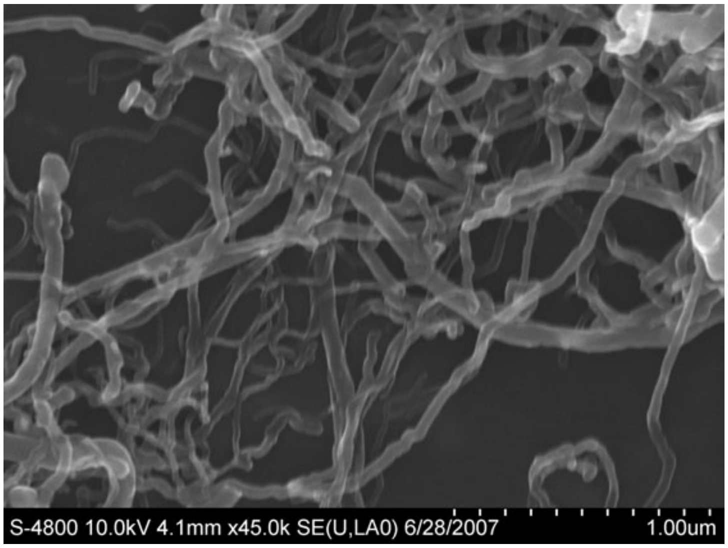

Figure 4.1: SEM image of carbon multiwalled nanotubes (tangled). X-ray diffractograms showed only carbon peaks for the precursors.

transparent and uniform in density. The nanotubes seem to be tangled up, yet each nanotube is still individual and can be traced as a single entity of approximately uniform diameter along its length. The ends are rather insignificant and the carbon tubes just stop abruptly. Although the tubes are not straight, the curves are round and the surfaces are even, changing direction gradually along a fairly smooth curve. One has the impression that the individual nanotubes could be separated without too much trouble (this is not true–due to strong Van der Waals forces, the nanotubes cannot be easily separated). They do not seem to be attached to each other or knotted up, and there is very little branching of one nanotube into two or more nanotubes.

The inside of the tubes are hollow with core diameters of 5-10 nm as shown in the higher magnification HRTEM image Figure 4.2. Again the nanotubes seem to lie across one another, but are still seen to be individual tubes. The striping along the outer surface is an interesting feature not seen in the lower magnification images.

Sample TFA1, which was sintered at 1200°C for 1 hour, shows growth of SiC with the same shape and morphology as the precursor carbon MWNTs (compare Figures 4.1 and 4.3). This growth was identified by x-ray diffractograms before post-treatment burning which showed that in addition to MWNT, there was some SiC present, see Figure 4.4.

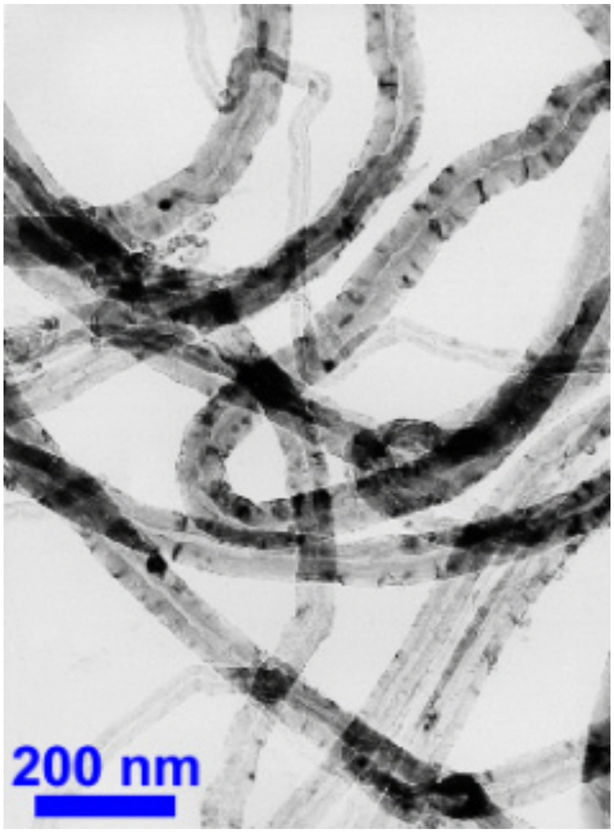

Figure 4.2: This high magnification HRTEM image of carbon multiwalled nanotubes shows more internal and external detail. (http://www.nanoamor.com/home)

Figure 4.3: HRSEM image of tube furnace sample TFA1 sintered for 1 hour at 1200°C shows morphology similar to starting material, tangled MWNT. Raman spectra showed that these are SiC nanotubes with a coaxial structure of a SiC surface shell surrounding a carbon nanotube, which is still hollow.

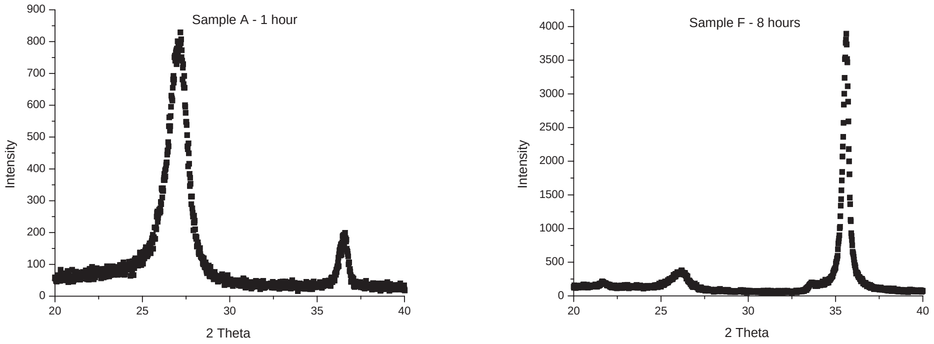

Figure 4.4: Comparison of XRD of samples TFA1 (sintered for 1 hour) and TFA8 (sintered for 8 hours) show that SiC is produced after only 1 hour of sintering, but after 8 hours sintering, almost all carbon is reacted, producing solid SiC nanowires.

4.3 Post-treatment Burning

For SEM and TEM analysis of SiC, specimens free of carbon nanotubes were needed. This was done by post-treatment burning, which removed the excess carbon in the induction furnace samples, leaving only SiC as shown by diffractograms before and after burning in Figure 4.5. See Figure 2.4 in Chapter 2 and discussion for details regarding post-treatment. X-ray diffractograms did not show evidence of remaining C after post-treatment. However, Raman spectra for TFA1 (the tube furnace sample with 1 hour reaction time) showed peaks at 1580 and 1350 cm^{-1}, indicating the presence of carbon nanotubes in addition to SiC peaks. Sample TFA1 contained MWNT even after post-treatment burning at 700°C. This result was confirmed by an FTIR study which also showed the presence of characteristic peaks due to carbon nanotubes at 881 cm^{-1} (Ref. [30]), 1422 cm^{-1}, and 1643 cm^{-1} (Ref. [31], [32]).

Previously, Menon, et al.[33] reported synthesis of SiC nanotubes and Wieligor, et al.[34] observed coaxial structures with a carbon core surrounded by a SiC outer shell. The most reasonable conclusion is that after 1 hour of sintering, a SiC layer coated the MWNT and prevented oxygen from reaching the interior of the tube to react with carbon, thus leaving SiC nanotubes with carbon cores. However, for samples sintered in the tube furnace for times longer than 5 hours and subsequently heated in air to 700°C or 1050°C K, x-ray diffraction, Raman and FTIR spectra did not show peaks characteristic to MWNT, indicating that these samples were solid SiC wires. Raman spectra and FTIR studies are discussed in Chapter 5.

In Figure 4.3, the SiC coated tubes are seen to lie across one another, but individual wires are still traceable just as in the pure MWNT image. The wires still look transparent, but the diameters of the largest nanotubes are now slightly larger than 100 nm. The ends are for the most part unremarkable, the changes in direction are mostly along smooth curves, and there is very little branching or evidence of any structure other than SiC coating the nanotubes themselves.

At higher magnification by HRSEM (see Figure 4.6), the surface and the inside of the wires are seen to be of different densities. The outer surface shows some higher density striping as

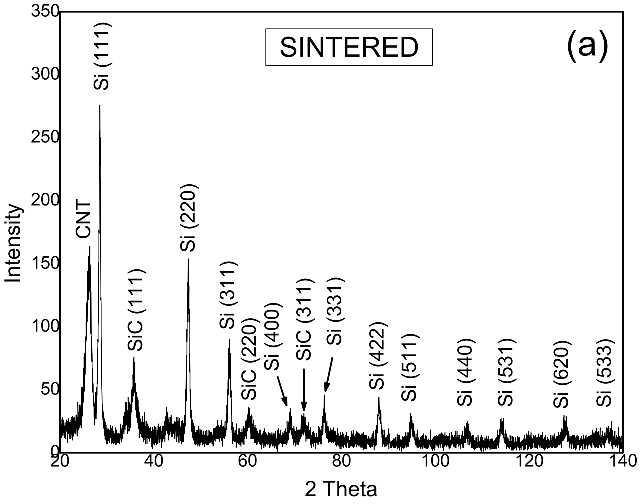

(a)

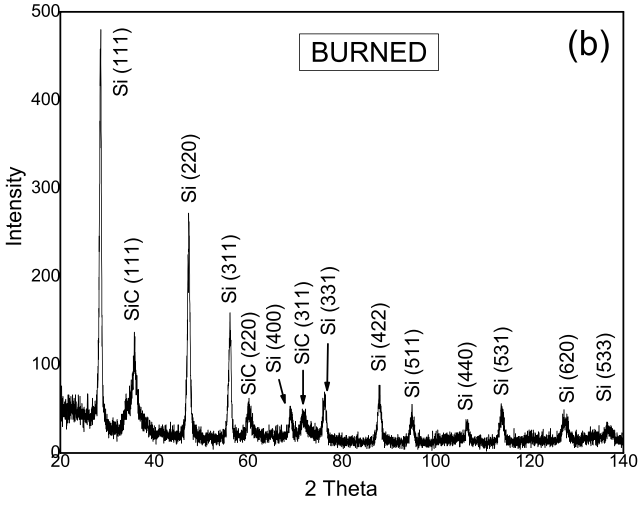

(b)

Figure 4.5: XRD before and after burning show that post-treatment is effective in removing excess carbon from the product.

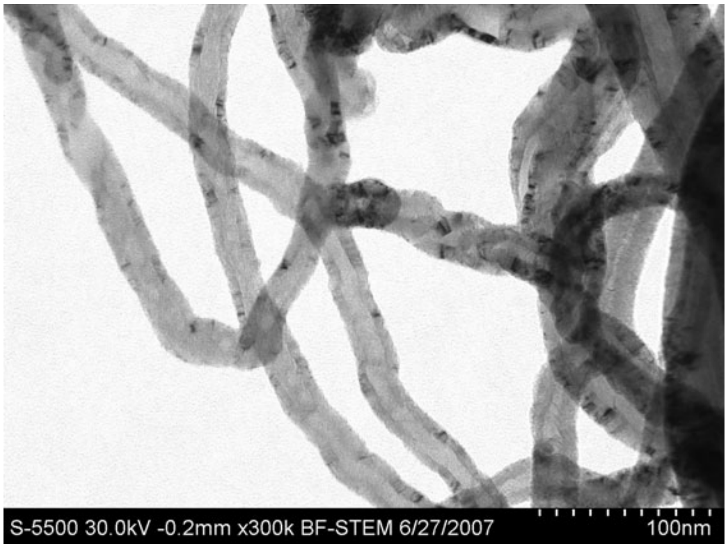

Figure 4.6: HRSEM image of tube furnace sample TFA1 sintered for 1 hour at 1200°C.

was seen on the MWNT at higher magnification, but here the surface is identified (again by XRD) as SiC. The inside is a hollow carbon tube, as confirmed by Raman spectrographs and FTIR spectra, but clearly differs from the outer walls in structure. It is speculated that the very inside is hollow since the starting MWNT are hollow and the images of Sample TFA1 are very similar to the images of the MWNT. The SiC nanotubes are still tangled, retaining the morphology of the original carbon nanotubes, and some tubes appear to twist along their length and to twist around each other. Still individual tubes apparently maintain their independence at this stage, and again there is very little evidence of the branching, which is characteristic of longer sintering times, and the changes in direction are generally along relatively smooth curves.

4.4 Progress of Reaction in 3 Hours

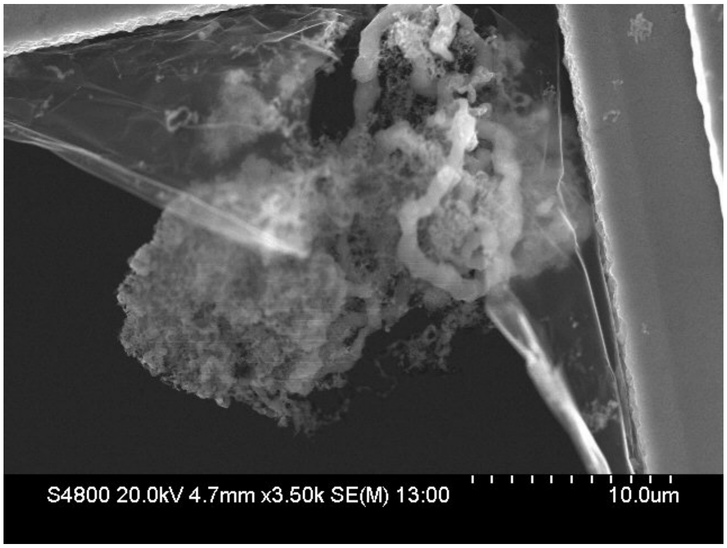

Figure 4.7: SEM image of this sample sintered for 3 hours shows progression of the reaction producing solid wires, some of which are beginning to fuse together.

Figure 4.7 shows a SEM image of Sample TFA3, which was sintered in the tube furnace for 3 hours. In this picture, several different types of growth can be recognized. The clump that looks tangled up is actually many SiC nanowires that were left after post-treatment burning. In the clump, the wires are difficult to distinguish individually and some of them are beginning to fuse together into thicker structures. Among the tangle of wires, several very large cylindrical tubes are seen. All the wires maintain the basic shape of the original nanotubes, but some have grown to huge diameters, up to 1.2 μm, and the bending and sharp elbow-like peaks begin to appear at this stage. See for example, SEM image in Figure 4.8.

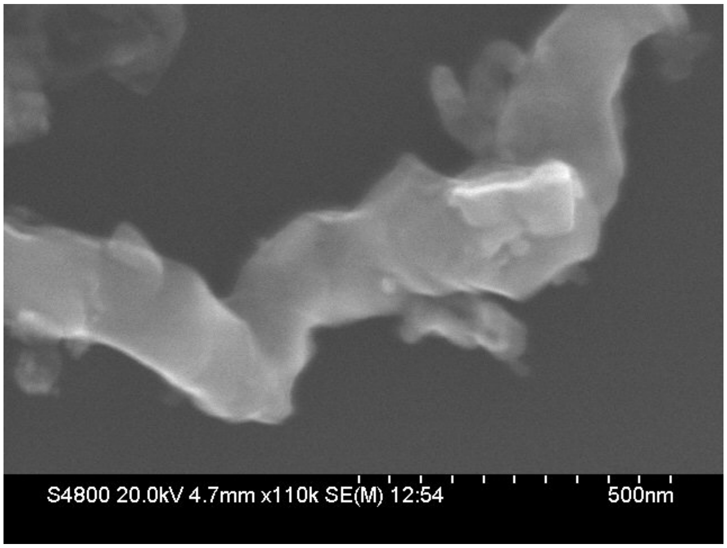

Figure 4.8: Wires in Sample TFA3 (SEM), sintered for 3 hours, have sharp kinks and grow to larger diameters than those sintered for less time.

In Figure 4.9, SEM shows that the morphology of another region of Sample TFA3 (reaction time 3 hours) looks quite similar to the original nanotubes and to Sample TFA1 (reaction time 1 hour) (Compare Figure 4.1 and Figure 4.3). The transparency of the wires is still a dominant feature, but several differences are obvious.

Some wires are not uniform along the length of a single wire, and there is some evidence of fusion of wires in the upper right-hand corner of the image. The outer diameters of the largest wires produced after 3 hours are larger than the diameter of the largest wire produced by 1 hour sintering (175 nm), see Figure 4.9. Many of the largest diameters in Sample TFA3 are 250 nm to 300 nm, with a few wires having diameters up to 1.2 μm (not shown in this image). The most significant feature in Figure 4.9 is the obvious knob-like structure near the center of the image, which is 270 nm across. This structure is shown at higher magnification in Figure 4.10.

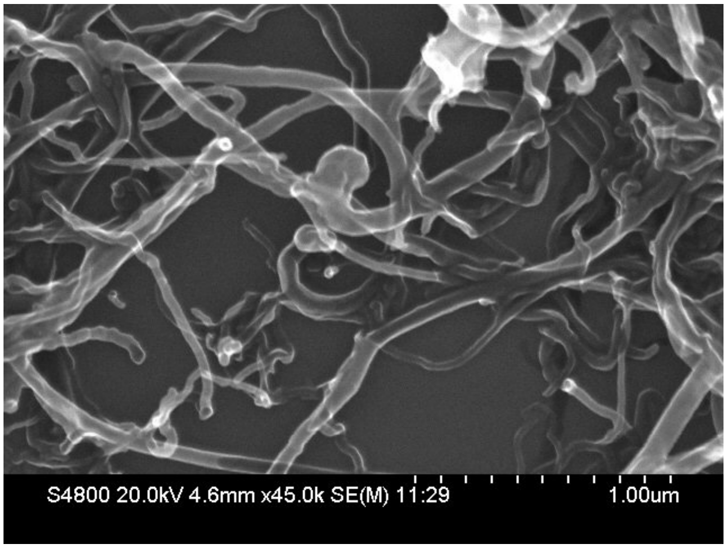

Figure 4.9: SEM image of Sample TFA3 (reaction time 3 hours) has similar morphology to precursor MWNTs and Sample TFA1 (reaction time 1 hour), but some wires have much larger diameters after 3 hours.

As sintering time increases, these enlarged structures on the ends of some nanowires become larger and larger and some have growths on the knobs that resemble flowers, see Figure 5.3(b) in Chapter 5. At the same time, the ends of some wires do not show this type of growth and remain unremarkable as in the original MWNTs. In Figure 4.10, the first stage of this type of growth is observed by SEM. This one appears to be the end of two different nanowires, joined together. The shading shows the interesting structure of the knob in some detail. These growths were not observed at shorter sintering times.

4.5 Progress of Reaction in 6 Hours and 8 Hours

Sintering for 6 hours (Sample TFA6) produced wires of even larger outer diameters, many up to 530 nm, with the general shape of the original MWNTs, but with much more variation in size and shape. For the first time, long very straight wires with smooth surfaces are seen somewhat randomly distributed among the tangled wires, see SEM image in Figure 4.11.

The sharp elbows and kinks as the tangled wires change direction are obvious by now. Note the twisting and three-dimensionality of these nanostructures. The transparency is gone, and

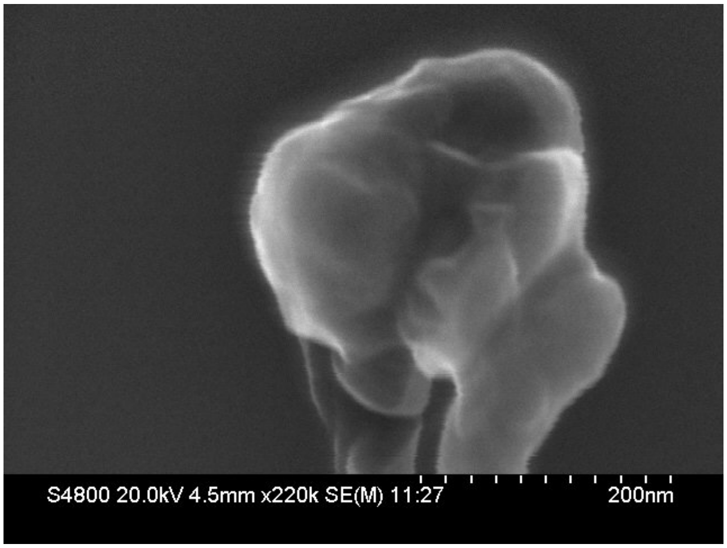

Figure 4.10: The interesting structure shown in this SEM image of Sample TFA3 is in an initial stage of growth.

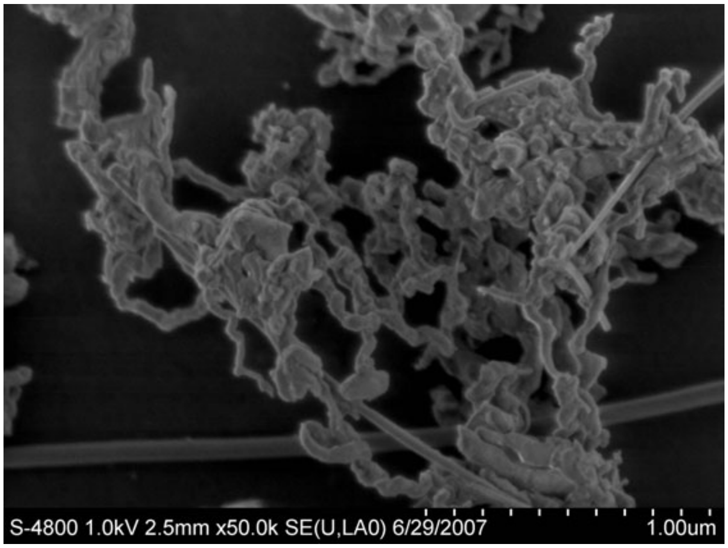

Figure 4.11: This SEM image of Sample TFA6 clearly shows the progression of the reaction to the formation of solid wires fused together into larger structures.

the more twisted and tangled regions are fusing together into much larger structures that are no longer wire-like. At the same time, several individual wires are noticeable, some smooth and straight and some kinky and curly. In the center of the image near the bottom, a knobby end is strikingly different than other ends in the same group that are just blunt ends with no difference in size from the wire itself.

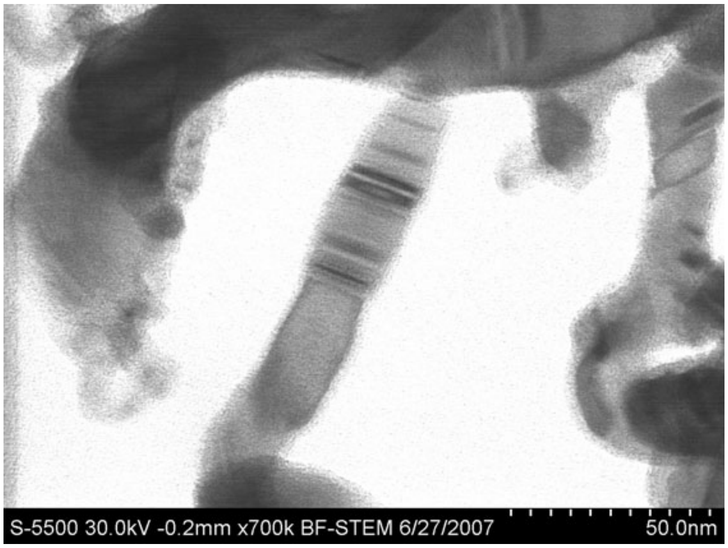

Figure 4.12: SiC nanowires produced after 8 hours sintering are shown in this HRSEM image of Sample TFA8. Striping indicates stacking faults in the crystal structure inside solid nanowires.

In Figure 4.12, the image shows Sample TFA8 (sintered for 8 hours) at higher magnification with HRSEM. Here the crystal structure inside of the nanowires is obvious, including stacking faults indicated by the high density striping. Discussion of these stacking faults can be found in Chapter 5. The nanowire in the center of the image is fairly smooth and straight, but the nanowire at the right seems to be twisted or kinked right at the point where the stacking faults occur. Note also that the outer wall looks different than the interior. At this point, the surface layer is amorphous silica formed during post-treating heating. The twisting and kinking could be a result of thermal expansion of precursors and product having different thermal expansion coefficients.

In the same way that a bimetallic strip is used in thermostats to detect the temperature change by measuring relative length changes for the two metals, the silicon condensing at the surface of a nanowire, for which the outer layer is now silicon carbide, may not stretch or shrink at the same rate as the outer layer, thus causing the silicon carbide to bend or kink as the silicon diffuses through the product phase at the surface. A similar circumstance could occur inside the tube while the reaction is occurring at the boundary of the product phase and the walls of the carbon nanotubes.

4.6 Results of Long Sintering Times

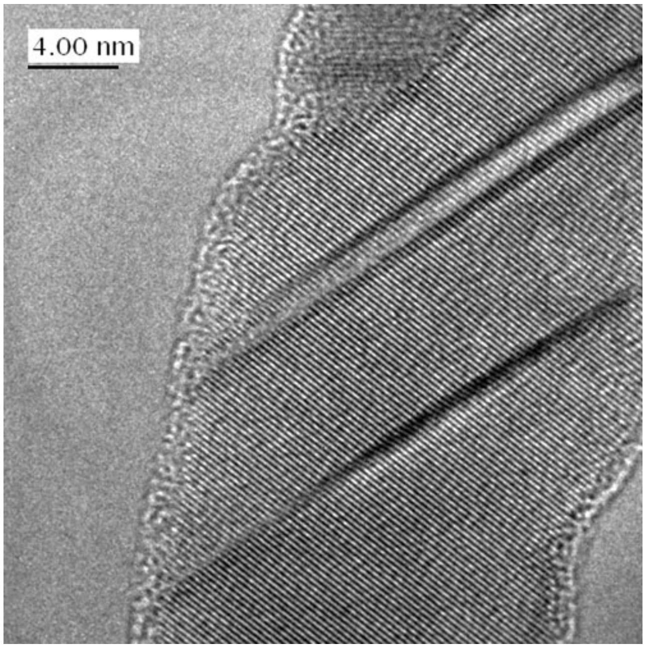

Figure 4.13: HRTEM picture of an individual SiC nanowire obtained after 64 hours of sintering at 1200°C in a conventional oven. Amorphous silica is seen as a 1-2 nm thick layer coating the nanowire. The diagonal lines are stacking faults.[35]

The HRTEM image of Sample CFA64 in Figure 4.13, which was sintered for 64 hours in a conventional surface, clearly shows internal structure similar to the HRSEM image of Sample TFA8 in Figure 4.12, including obvious stacking faults. The amorphous surface layer confirms the lack of structure at the surface of the produced SiC nanowires. Dramatic changes in the structure and morphology were observed when sintering time reached or exceeded 3 hours. The structure of the product is discussed in more detail in Chapter 5.

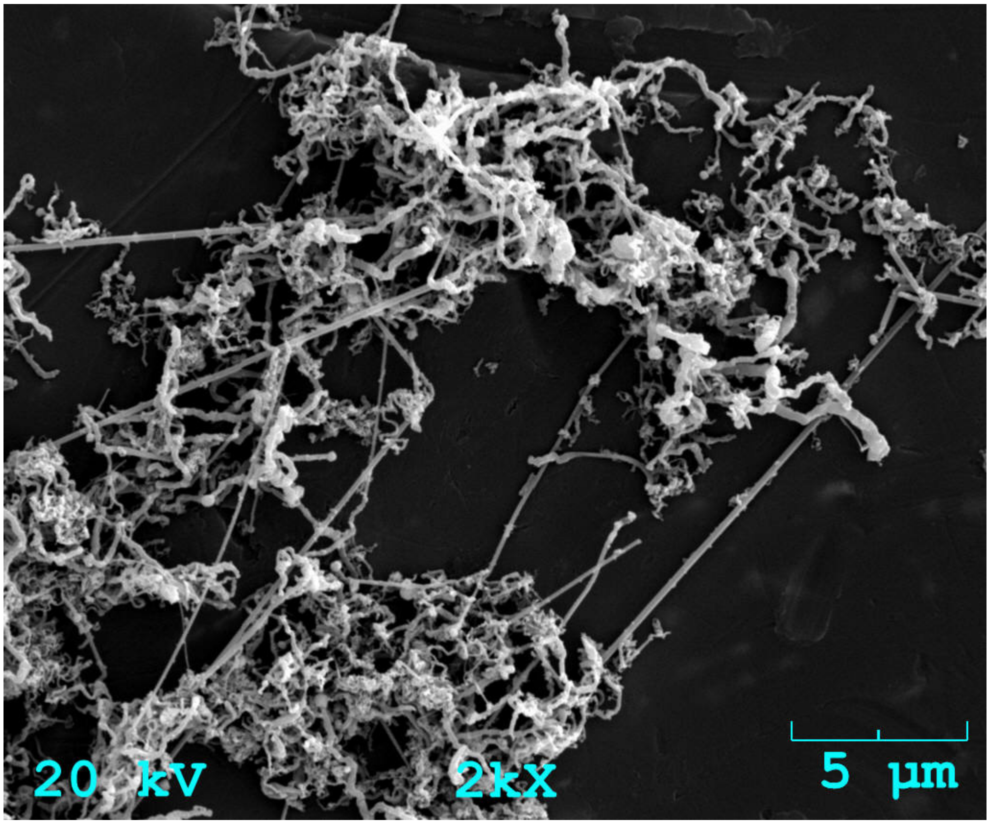

Figure 4.14: SEM image of Sample TFB20, sintered for 20 hours and produced from precursor aligned MWNT.

Longer sintering times (20 and 26 hours) were also done for comparison and to find the reaction time for the complete reaction, but it must be noted that Sample TFB20 in Figure 4.14 was produced from aligned nanotubes rather than tangled MWNTs as before. This SEM image shows more long straight wires among the clusters of curly wires after 20 hours sintering, but overall the nanowires produced are still a tangled mess. Some evidence of the fusion of nanowires to each other is also evident here. The ends of several nanowires are visible in this image, and it is notable that some have plain blunt ends and some have knobby ends. The long straight wires tend to be smaller in diameter than the average wire in this sample. Note the range of diameters continues to increase with sintering time. The samples sintered for 20 hours, 26 hours, and 64 hours still have many small wires of diameters 30 nm to 40 nm but they also have an increasing number of large wires with diameters 500 nm to 1 μm.

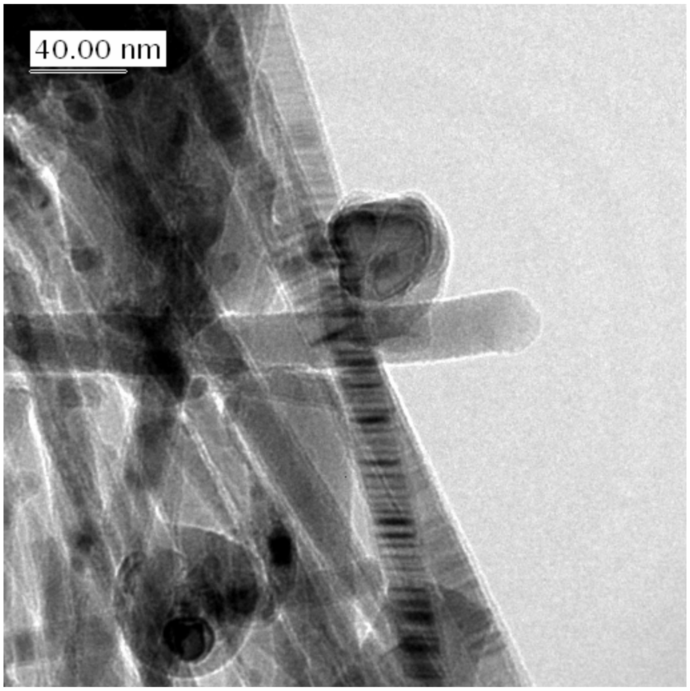

Figure 4.15: Crystal structure, stacking faults, wire straightness and alignment are striking features of SiC nanowires in this HRTEM image of Sample TFB20, sintered for 20 hours and made from aligned MWNT. There are also many wires completely free of stacking faults.

Viewing Sample TFB20, the 20 hour sample, with HRTEM, demonstrates the knobby growths on the ends of some, but not all wires. In addition, the crystal structure inside the wires becomes a dominant feature of SiC nanowires produced with longer reaction times. See Figure 4.15. The amorphous surface layer is visible in most wires in this image. The fact that all the wires in this image appear to be fairly straight and uniform, along with more wires completely free of stacking faults, is attributed to the starting material used, which were again aligned MWNTs.

Sintering for 64 hours was done to find the total reaction time at this temperature, and indeed the reaction appears to be essentially complete at this time. The x-ray diffractogram indicates that there is no excess carbon in the produced silicon carbide for this reaction time. This sample, produced from the tangled MWNTs, includes SiC nanowires of a wide range of diameters tangled together, sometimes looking braided. The ends of some wires are enlarged knobs as was observed in other samples. A few straight wires appear in a jungle of kinked

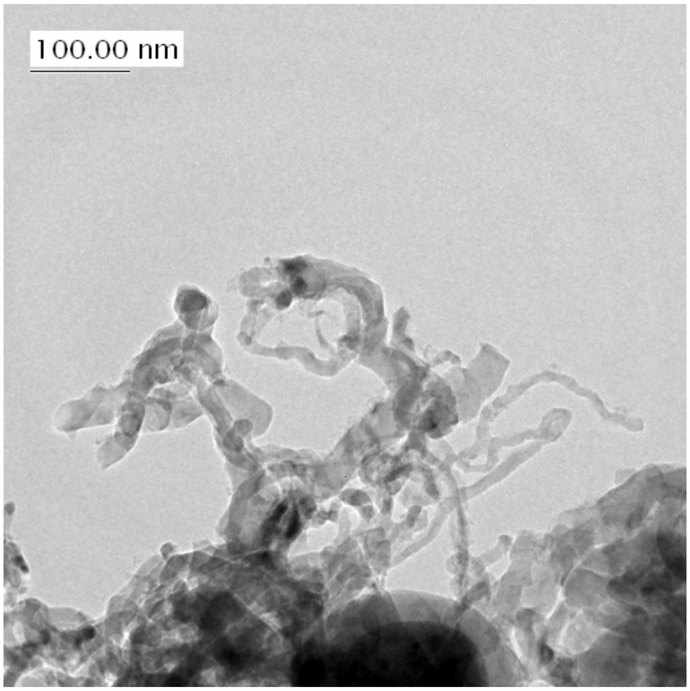

Figure 4.16: The reaction is complete, and the product is a mixture of SiC nanowires of different sizes and shapes as shown by HRTEM.

and twisted curly wires, see Figure 4.16. Measured diameters of the nanowires in this sample were as large as 800 nm, with the smallest ones still being less than 30 nm. It is speculated that the sample probably has wires with diameters larger than 1 μm since wires this large were discovered and measured in other samples with reaction times as short as 3 hours. There are very few smooth curls in this sample. Most of these nanowires are kinked and bent in different directions. The wires are entangled and it is much harder to distinguish individual wires in this sample. Many appear to branch into multiple wires or to be fused together at different points along the wire.

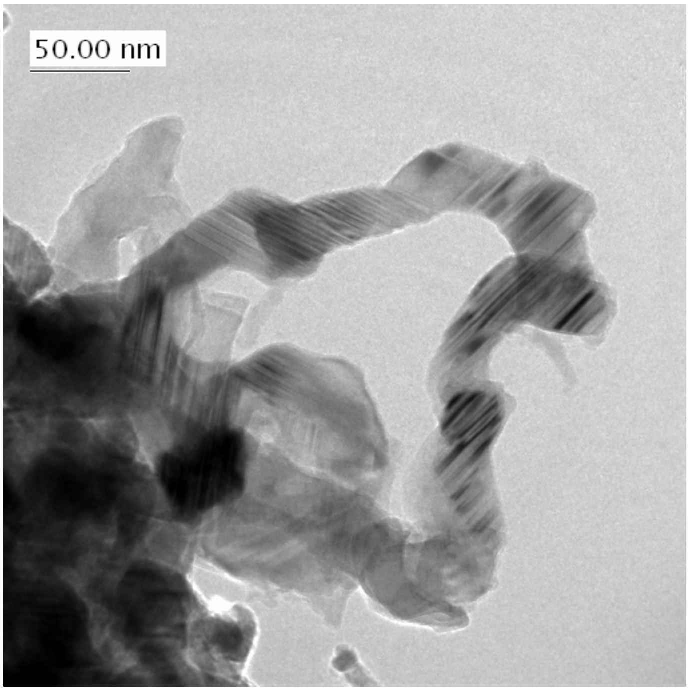

Figure 4.17: In the SiC nanowires produced in the complete reaction, there seems to be crystal structure everywhere in these solid wires, including dominant stacking faults.

A closer look showed an abundance of stacking faults, implying definite crystal structure inside most wires after sintering for a time interval equivalent to the complete reaction time, as shown in Figure 4.17. It is remarkable that the stacking faults showed layering along one direction, despite the kinks and changes in direction of the nanowire itself. Here some other fused nanostructures can be seen, but stacking faults appeared to dominate everywhere. More discussion of stacking faults can be found in Chapter 5.

4.7 Morphology and Reaction Mechanism

As described in Chapter 2, Si powder was used as a reactant for 4 different carbon precursors: tangled MWNT, aligned MWNT, SWNT, and carbon nanograss. The analysis of the morphology for various sintering times was done for the product formed with tangled MWNT, and the morphology of the product formed from aligned MWNTs was included since it fit well in the time progression. Clearly, much more information could be gained by doing a similar complete analysis for the other carbon precursors.

Initially, silicon carbide nanotubes were produced having an outer shell comprised of SiC, an inner core of carbon and a hollow interior remaining from the initial MWNT. The produced nanotubes had slightly larger diameters but retained the shape of the starting material, thus resembling the pure MWNTs. The largest SiC containing tubes were more than 100 nm in diameter (100 nm represents the upper limit for the outer diameter of the MWNT precursor). The SiC structures produced after only 1 hour of sintering continued to be rather transparent and appeared to be of similar density and structure to the precursor MWNTs. A higher magnification showed that the interior of the cylinder differed from the outside shell. Because it looked similar to the images of the MWNT, it is likely that the interior of these nanowires was hollow as well. This coaxial structure was confirmed by Raman and FTIR studies.

As sintering time increased beyond 3 hours, not only did the outer diameters of the largest wires continue to grow to phenomenal sizes (up to 1000 nm), the shape of the wires themselves began to change. They began to appear as solid SiC wires without a hollow interior. A majority of the structures continued to have small diameters, less than 30 nm, but the morphology of the wires with increased size showed evolution into very different structures. What were initially curls with rather smooth curves began to be sharp elbows and kinks. The ends became nuclei for further growth, and the outer surfaces began to look flaky and layered. After long sintering times, the inside of the wires showed clear crystalline structure, including stacking faults. Many of the wires became fused together into large structures that showed only a hint of the original cylindrical shape.

The x-ray powder diffractogram of Sample TFA1, after post-treatment burning at 1050°C for 2 hours, showed only β-SiC peaks, indicating no carbon nanotubes were left in the sample. The x-ray diffraction peaks were slightly broadened, which was expected as an indication of small diameter wires, but no shoulders were seen. This indicated that the nanowires have the cubic crystal structure suggested by the location of the peaks, but no stacking faults were observed. Raman peaks and FTIR peaks indicative of carbon were opposing findings suggesting that the outer layer was pure SiC, but carbon remained inside the SiC shell and was unseen by XRD.

This first hour of sintering then was a simple vapor-phase reaction with vaporized silicon going to the MWNTs and reacting with the carbon atoms near the surface to form a silicon carbide shell surrounding the MWNTs. This would explain why the outer diameter grew. Carbon must have diffused through the boundary phase of SiC product and reacted with silicon vapor at the surface of the outer wall. It is well known that nanotubes often have dislocations and defects in the crystal structure. Those dislocations appear as high density regions where the stacking layers were off by one atom. Refer to Chapter 5 for models of stacking faults. The striping along the outer surface may be evidence of the crystal structure of the nanotubes or it may be evidence of the crystal structure of SiC forming at dislocation sites on the nanotubes.

XRD of TFA3, sintered for 3 hours, (after post-treatment) showed a slight shoulder on the [111] peak of SiC, which confirmed the presence of the stacking faults observed in the SEM images. Analysis of x-ray diffractograms of all samples indicated that the stacking faults began to appear after 3 hours of sintering and continued to be more prevalent as sintering time increased. In the post-treatment x-ray diffractogram of Sample TFB20 shown in Figure 4.18, in which aligned MWNT were used as a precursor, the shoulder on the [111] peak is marked with an arrow. The more pronounced shoulder is an indication of the abundance of stacking faults, which were observed by HRTEM images of this sample.

Refer back to Figure 4.4 and note that Sample TFA1 showed no evidence of stacking faults in the SiC [111] peak, but Sample TFA3 had a slight shoulder. The shoulder in the x-ray peak of SiC [111] appeared at the same reaction time that stacking faults in the SEM images were first observed.

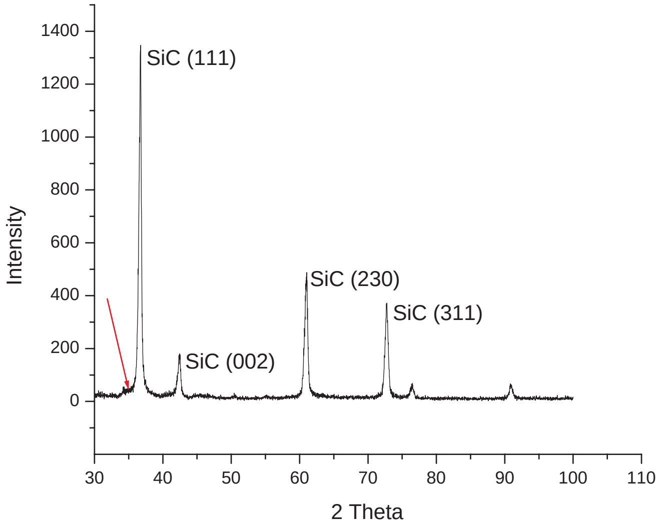

Figure 4.18: XRD of Sample TFB20 for which many stacking faults were observed by HRTEM. Stacking faults are indicated by the pronounced shoulder marked with an arrow. Note also that all excess carbon has been removed by post-treatment burning (confirmed by Raman and FTIR spectra).

The crystal structure of the interior of SiC wires produced by 3 or more hours of sintering indicated the presence of a solid-solid reaction, where Si has condensed at the surface and diffused through the SiC product phase to the inner layers of C to form crystalline SiC inside the tubes. Recall that the initial reaction indicated diffusion of carbon through the product phase to interact with silicon vapor at the surface of the outer wall. Clearly, both precursors must have diffused through the product boundary phase, and the reaction occurred at both boundaries of the product.

The knobs and growths as well as the apparent fusion of wires can only be representative of Si and C both reacting in the vapor phase and then attaching to the surface of SiC. Thus, there is evidence that (1) vaporized Si reacted with solid C, (2) solid Si reacted with solid C (inside), and (3) vaporized Si reacted with vaporized C. Together these implications provided a wealth of information regarding details of the diffusion-controlled reaction that successfully produced pure SiC nanowires.

The stacking faults shown by HRSEM in Figure 4.19 are clear evidence of crystal growth inside the tube and that growth was always in the direction of the [111] plane. The reaction must have proceeded by diffusion of Si through the growth layers of SiC to react with the carbon inside the MWNT.

Figure 4.19: In this HRSEM image, Sample TFA3 shows clear crystalline structure inside the SiC nanowires.

It is also interesting to note that not all structures formed were cylindrical in shape. After only 1 hour, flakes were also seen with a crystalline outer layer on both sides and a layer of what appeared to be misshapen or deformed nanotubes sandwiched between.

This structure also indicated that growth occurred by Si vapor reacting with carbon nanotubes at the outer wall of carbon, see SEM in Figure 4.20. The transparent sheet showed a layered structure where SiC nanowires began to fuse together, with a layer in the middle that looked like deformed nanotubes. From this early stage it is not hard to imagine the collapse of this type of structure after longer sintering times producing the large structures seen along with the solid nanowires, for example, in Sample TFA6 in Figure 4.11.

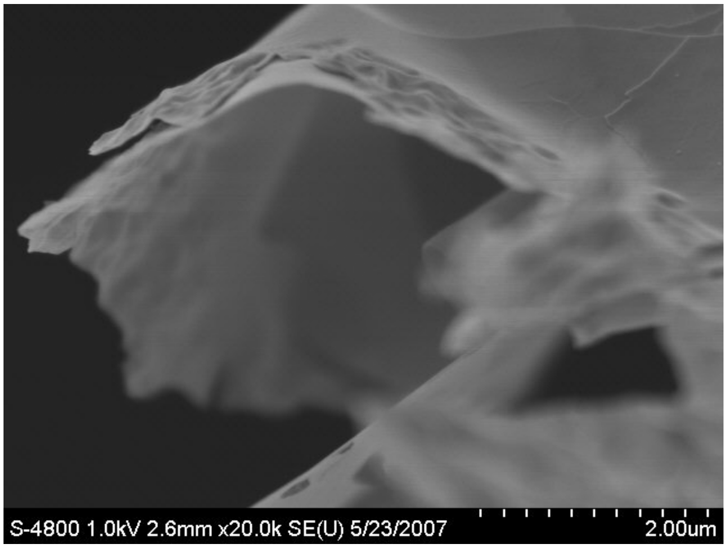

Figure 4.20: The layered structure is shown at the end of a SiC nanotube from Sample TFA1 in this SEM image.

4.8 Size Distribution

One obvious effect of allowing the reaction to continue until it was complete was the growth in diameter of the produced SiC nanowires. Beginning with the diameter of the precursor MWNTs, the outer diameter of the hollow nanotubes and then the solid nanowires increased as the reaction progressed. However, it was noticeable that for all reaction times, very small diameter wires were still present, no matter how large the largest nanowires were.

From SEM and TEM images for samples TFA1 and TFA6, the diameters of the nanotubes and the nanowires were measured, and the size distribution was plotted. Experimental data were fitted to lognormal distribution functions and the results are shown in Figure 4.21. The precursor MWNTs had a mean diameter of (46 ± 18) nm. The mean diameter of SiC nanowires increased from 59 nm for one hour reaction time with geometric standard deviation 49 nm to 113 nm with geometric standard deviation 97 nm for six hours. It was found that once growth began, all samples contained tubes or wires with a range of diameters. The plot shows that not only did the diameter of the largest wire increase with increasing reaction time, the mean diameter also shifted to a larger value with increased reaction time, and the width of the distribution expanded significantly. The Scherrer equation, Equation 2.2 in Chapter 2, was

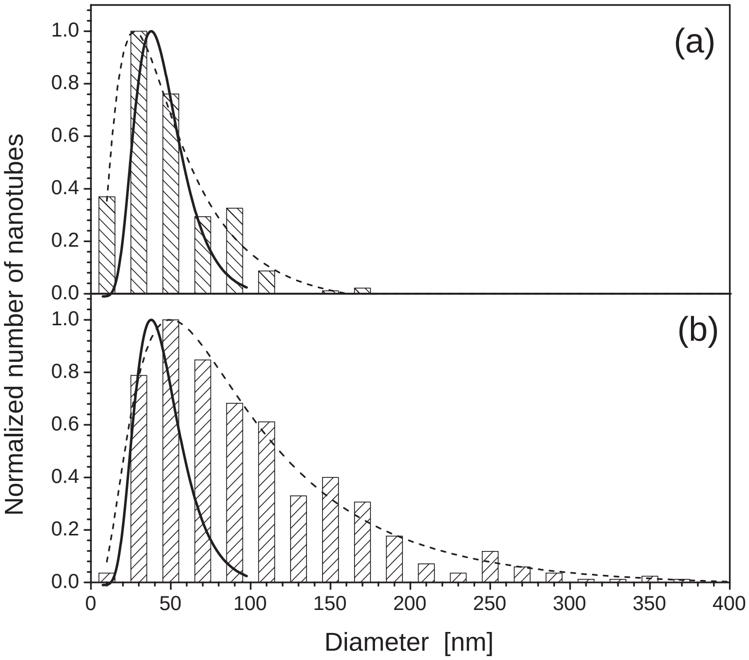

Figure 4.21: Fitting of lognormal distribution function to normalized distribution of SiC nanowires diameter: (a) SiC nanotubes after 1 hour of sintering had average diameter (59 ± 49) nm, (b) SiC nanowires after 6 hours had average diameter (113 ± 97) nm. The bold solid line is for the distribution of the precursor MWNT, average diameter (46 ± 18) nm. Note that error values represent geometrical standard deviations for lognormal distributions.

used to find the crystallite size from the broadening of XRD peaks, which were determined to be about 30 nm. The discrepancy with these measurements is interpreted to mean that for longer sintering times where stacking faults dominate, the Scherrer equation reflects the distance between stacking faults. A more detailed line profile analysis of the XRD data would determine the meaning of the different numbers.

Chapter 5

Structure of SiC Nanowires

5.1 Production of Silicon Carbide Nanowires

Silicon carbide nanowires have been produced by many different methods, such as catalytic chemical vapor deposition,[36] vapor-liquid-solid growth mechanism,[37] sol-gel processes,[38] reaction between carbon nanotubes (CNT) and SiO vapor at high temperatures,[39] reaction between CNT and liquid or vapor Si,[34] and others.

In previous studies at TCU, Wieligor, et al., synthesized SiC nanowires by mixing CNT and silicon nanopowder followed by heating to temperatures between 1000°C and 1450°C and then applying pressure between 2 and 8 GPa.[34] This method resulted in SiC in the form of nanowires and nanosize grains mixed together. SiC nanowires obtained at low temperatures had small diameters, less than 50 nm, while those obtained at high temperature had larger diameter, usually 100 nm, and a coaxial structure with carbon nanotubes forming the interior and SiC the outer layers. Although pure SiC was obtained, its morphology was not uniform, and in addition to nanowires, nanosize grains were also produced. It was impossible to separate nanowires from nanosize SiC powder.

To avoid this complication the procedure was modified, and the tube furnace samples initially produced SiC nanotubes with the coaxial structure previously observed, but the nanosize grains were eliminated. For reaction times longer than 3 hours, pure solid SiC nanowires were produced from MWNT and Si vapor at 1200°C.

The SiC specimens discussed in this chapter are representative samples of the produced SiC nanowires. Sample CFA64, which was produced from the precursor tangled MWNTs A and sintered for 64 hours, and Sample TFB20, which was produced from the precursor aligned MWNTs B and sintered for 20 hours, see Table 2.1 in Chapter 2, have been selected for the comparison of structure produced from different precursors, as well as the general structure of all nanowires produced by the method of sublimation of silicon in the tube furnace. Discussion of Sample TFB26 is included when it displays a difference that is significant and relevant to the results. The chapter concludes with HRSEM image of one example, Sample TFA8, which demonstrates that the interior stacking faults and the amorphous surface layer were present at shorter reaction times, in this case 8 hours.

5.2 Crystal Structure

The x-ray diffractograms of produced SiC clearly indicated the presence of crystalline SiC with cubic symmetry. Figure 5.1 part A depicts the diffraction profile for Sample CFA64 and part B for Sample TFB20. In both patterns reflections due to the cubic phase of SiC are the main feature. Peaks typical for the hexagonal structure of SiC are pronounced in Sample CFA64 but only traces are noticeable for Sample TFB20. The silicon carbide peak is not as broad as expected with nanosize grains because all layers grow in the same direction [111], even though the wires may curl. For Sample TFB26, the XRD showed 2H structure similar to that of CFA64. No other crystalline structures were detected. The pattern of XRD peaks showed that as reaction time was increased, the abundance of stacking faults increased to the point of producing a separate 2H peak.

Figure 5.2 shows typical SEM images. Most abundant are short, twisted SiC nanowires of estimated diameters between 20 nm and 100 nm. In addition, numerous straight wires of

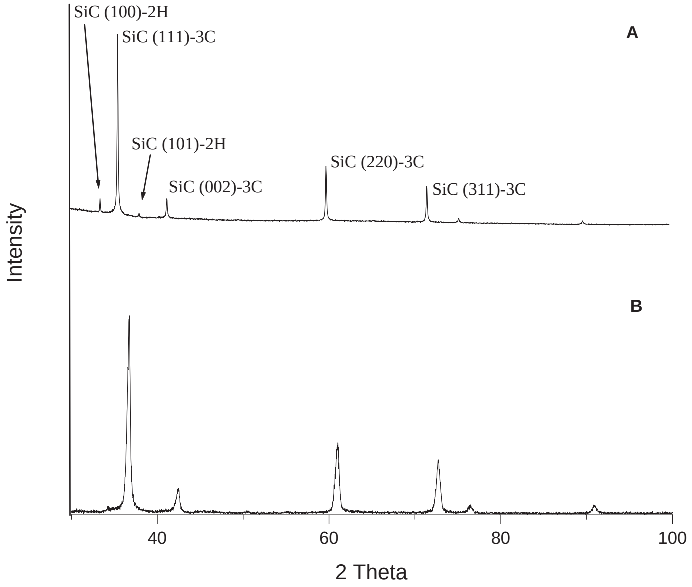

Figure 5.1: SiC obtained from precursors A (tangled MWNT) and B (aligned MWNT) shows crystal structure with cubic symmetry typical for β-SiC. Peaks denoted as 2H, indicated in Part A, are due to stacking faults present in the cubic structure and do not represent a separate hexagonal phase

lengths exceeding 30 μm and diameters ranging from 30 nm to 400 nm, sometimes even reaching 800 nm, are also present in the specimens. No differences in morphology of specimens produced from precursors A and B have been observed (compare SEM images in Figure 5.2 (a) and (b)).

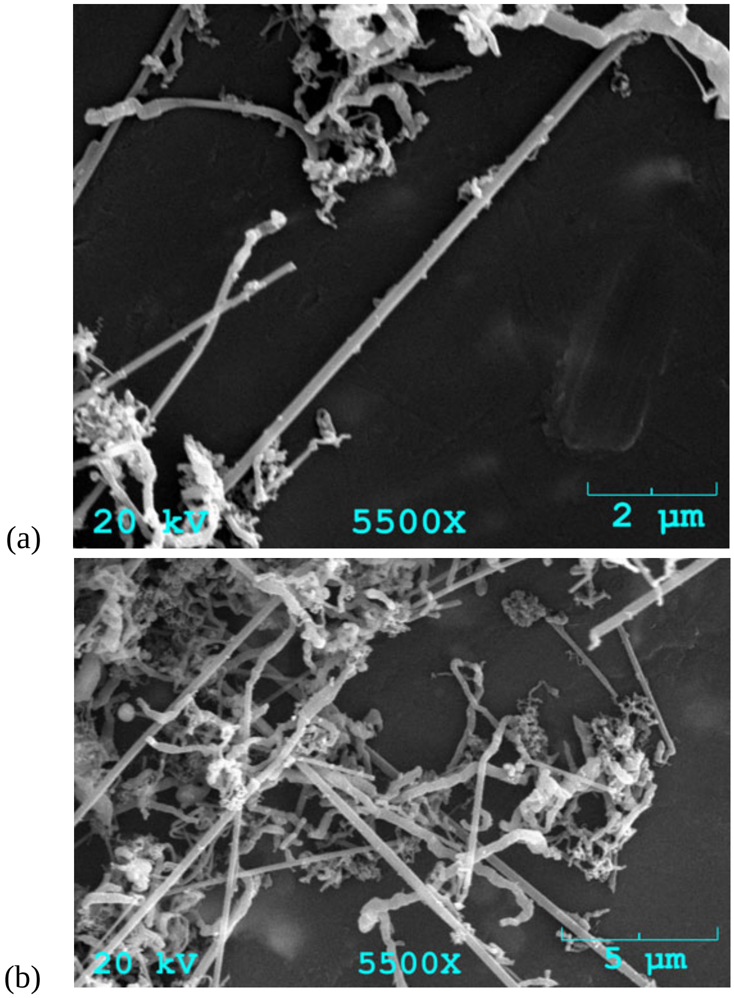

Figure 5.2: SEM images of SiC nanowires (a) Sample CFA64 made from tangled MWNTs A and (b) Sample TFB20 made from aligned MWNTs B demonstrate that no obvious differences in morphology were observed.

5.3 Stacking Faults

Stacking faults are crystal defects in which the normal stacking sequence is somehow interrupted or changed. For example, normally cubic layers are stacked ABCABC. Where there is a stacking fault, the layer may become ABCAB*ABC or ABCA*CABC. The asterisk denotes the place where the fault occurs and a layer is left out, creating either ABAB or CACA. In either case a layer of the cubic sequence is missing, and those few layers look the same as the hexagonal structure, ABABAB. The 2H structure observed in the diffractograms of the samples described in this chapter are thus to be interpreted as stacking faults that look the same as the 2H phase of SiC, rather than evidence of actual crystals formed with the 2H structure, which is rare and requires more energy to form.

Sample TFB20 showed only small peaks evident of the 2H structure in the x-ray diffractogram. TEM images showed a lot of straight wires that looked much nicer than those in CFA64, which is attributed to using the oriented MWNT reactant B. The x-ray diffractogram of Sample CFA64 showed a significant amount of SiC with 2H structure, indicating more 2H stacking faults in Sample CFA64, that is to say more stacking faults occur with longer reaction times and with lower quality precursors.

High resolution TEM images, examples shown in Figure 5.3, reveal a high concentration of stacking faults and the presence of an amorphous phase near the surface of the nanowires. Distribution of stacking faults varied with location within the nanowires, and stacking faults were abundant in small diameter wires, less than 30 nm. In TFB20 and TFB26 samples, a high concentration of nanowires free of stacking faults was observed. In Sample CFA64 and other samples produced from the same precursor tangled MWNT A, not only were stacking faults abundant, there were also numerous flower-like structures such as the one depicted in Figure 5.3(b) (HRTEM).

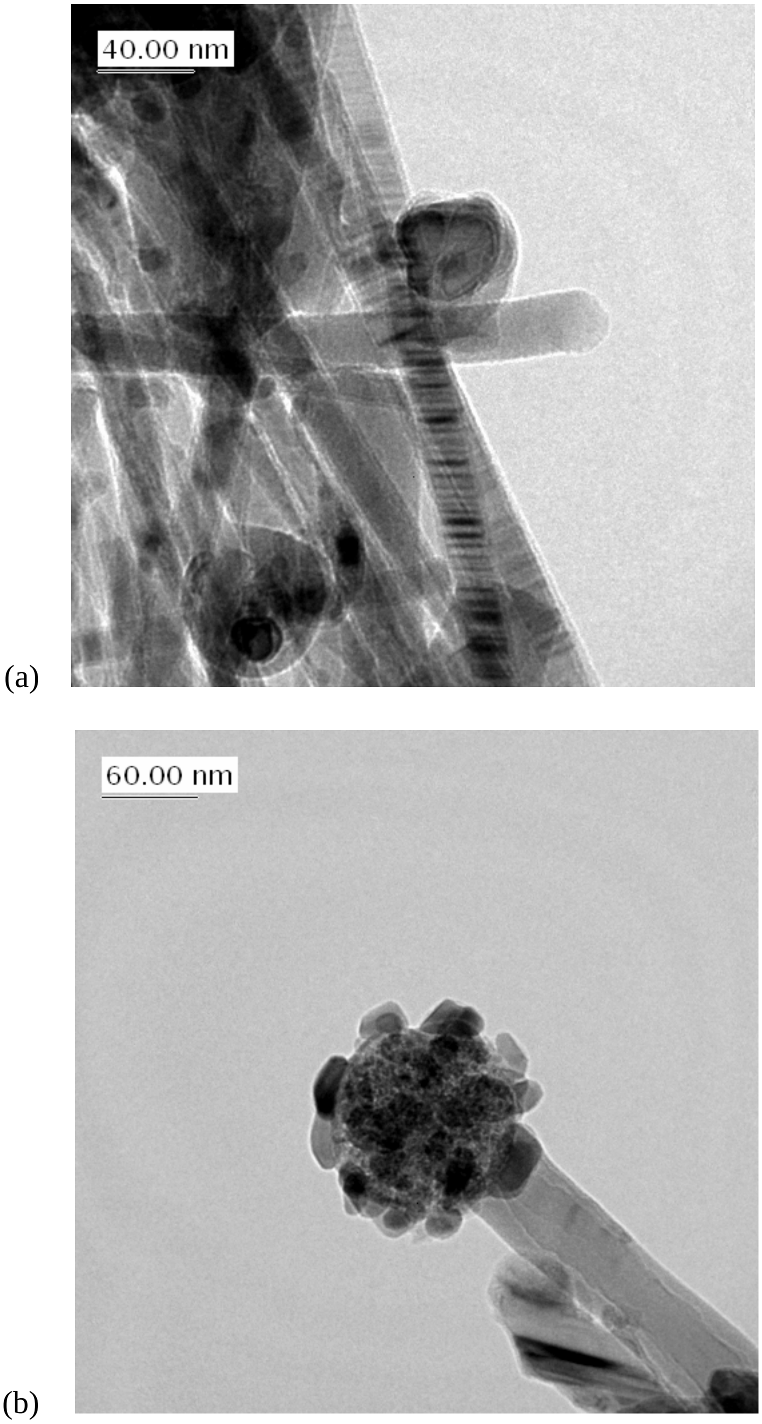

Figure 5.3: HRTEM images of SiC nanowires. (a) Stacking faults were abundant in small diameter wires, less than 30 nm. (b) Numerous flower-like structures were found throughout samples produced from precursor MWNT A.

5.4 FTIR Spectra

FTIR spectra of the specimens were similar, and an example is shown in Figure 5.4. In addition to the characteristic band due to the SiC vibrations at about 810 cm,$^{-1}$ a small peak at about 1100 cm^{-1} due to SiO and another peak, even smaller, near 1250 cm^{-1} due to SiO and/or Si-CH_3 groups were present. No other vibrations were detected.

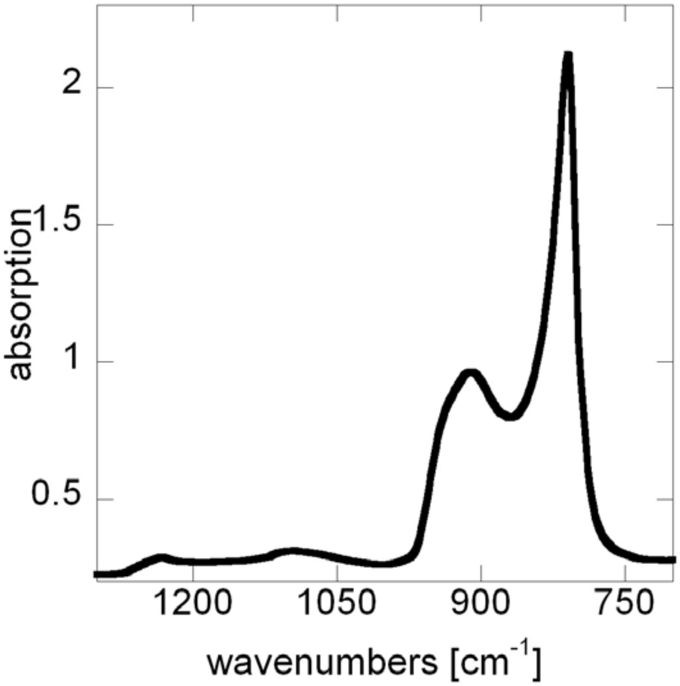

Figure 5.4: A representative FTIR absorption spectrum shows a small peak at about 1100 cm,$^{-1}$ which indicates the presence of SiO, and the smaller peak at 1250 cm^{-1} is due to SiO and/or Si-CH_3 groups. No other vibrations were detected.

The shape of the main infrared absorption peak shown in Figure 5.4 is typical for silicon carbide fibers.[40],[41] Two components can be distinguished: one centered at about 810 cm^{-1} and another at 910 cm^{-1}. Sasaki, et al.[41] explained the shape of the absorption contour in the 700 - 900 cm^{-1} region as a result of a coupling between optical phonons and plasmons. It was assumed that the particles were spherical and could be separated into a crystalline core and a disordered, charge-free shell. Consequently, the IR band has two components, one due to vibrations of atoms in the surface layer (broad, asymmetric band) and another due to phonons in the crystalline core (narrow, symmetric peak). Further it was assumed that the plasmon may exist only in the core. As the size of SiC grains decreases, the frequency of the optical longitudinal LO phonon, ω_{LO}, decreases, while that of the transverse phonon TO, ω_{TO}, increases. The relative contribution of the shell atoms increases with decreasing grain radius, and this effect is responsible for the diminishing difference (ω_{LO} - ω_{TO}), which results in more effective damping of the phonon.

Mutschke and coworkers[42],[43] offered an alternative explanation for the origin of the 910 cm^{-1} component. They postulated that this component is a result of relative polarization of the incident light and orientation of the nanocrystal. For elongated crystalline samples, such as long fibers, the 810 cm^{-1} band was shown to be polarized in the direction of the axis while the 910 cm^{-1} band was observed only when the electric field of incident radiation was perpendicular to the symmetry axis. In the case of the KBr pellets, they contained numerous randomly oriented and twisted SiC nanowires resulting in a wide distribution of angles subtended by the nanowires. This effect could explain the relatively large intensity of the 910 cm^{-1} band seen in Figure 5.4.

The low frequency side of the peak at 810 cm^{-1} can be approximated by a Lorentz function. Note that amorphous SiC results in a wide Gaussian band with full width half maximum approaching, in extreme cases, 200 cm^{-1}. Previous experimental works proved that when compositional disorder is introduced, i.e., SiC is not stoichiometric, or the sample contains foreign atoms, then a low frequency shoulder appears, and often its width is measured in hundreds of wavenumbers.[44],[45] In this case the 810 cm^{-1} peak is slightly asymmetric, but its shape could be reasonably approximated by a Lorentz function. The Gaussian component which accounts for inhomogeneous broadening was very small; therefore, it is assumed that the concentration of amorphous SiC was small.

5.5 Raman Spectra

Raman spectroscopy is less sensitive than FTIR and does not provide information on the concentration of foreign objects, but it has the advantage that it can be used to characterize the atomic structure of the sample. The cubic phase of bulk SiC shows two strong Raman peaks at 796 and 973 cm^{-1}, compare Figure 5.5. These are two phonon peaks and their intensities depend on the wavelength of the excitation light. For the 514 nm laser line, which carries energy close to the band gap energy in SiC of 2.4 eV, the TO peak is stronger than the LO counterpart.

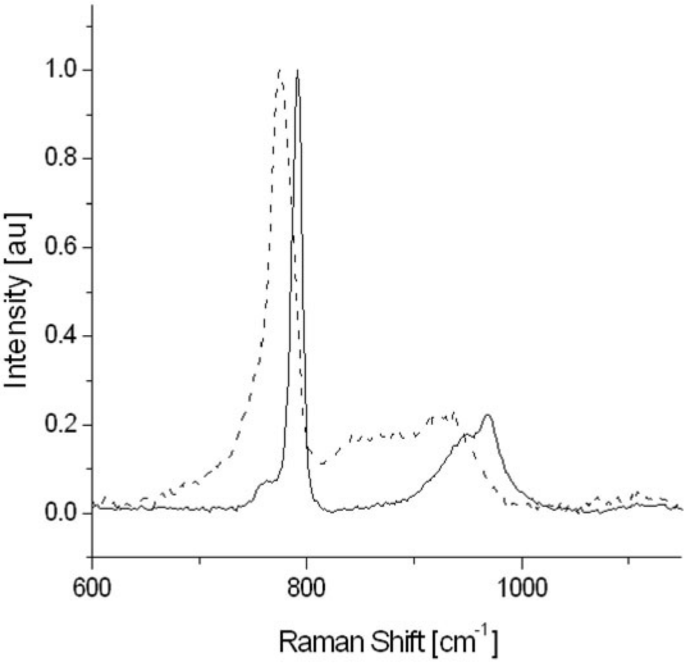

Figure 5.5: Typical Raman spectra collected for a cluster of SiC nanowires. The solid line is the spectrum for Sample TFB20, and the dotted line is the spectrum for Sample CFA64.

The hexagonal phase of SiC has Raman peaks that are slightly shifted, and a careful analysis of the frequency positions can be used to identify the crystallographic structure.[46] Raman microscopy allows recording spectra from a single nanowire, and Figure 5.6 shows spectra obtained at three different locations along the same nanowire selected from sample TFB20. The spectra are not identical and the relative intensities of the LO and TO components vary.

Like the morphology of samples described in Chapter 4, the morphology of these two specimens (CFA64 and TFB20) was not uniform; straight and curled wires, compare Figures 5.2 and 5.3, of diameters varying between 20 and 800 nm and lengths varying from tens of nm to tens of μm were detected. Despite significant differences in diameters of the starting material (carbon nanotubes A and B), the final products had comparable geometry and shape. Manufactured nanowires from precursors MWNT A and B had identical chemical composition and similar morphology and structures. X-ray diffractograms and Raman spectra showed only signatures typical for SiC. In addition to peaks related to Si-C modes, infrared absorption spectra included small peaks assigned to SiO and $SiCH_3$ vibrations. These groups are most likely present on the surface of the nanowires and probably were formed during the postproduction heat treatment at 700°C.

IR spectra are insensitive to the SiC phase, cubic vs. hexagonal, and appear to be only slightly affected by the confinement effect.[38],[42],[43] Therefore, IR spectra cannot be used for evaluation of the concentration of stacking faults or the size of nanowires. On the other hand, Raman spectra of SiC are well understood.[47],[48] For the cubic phase two phonon modes are allowed, and they appear in the solid line in Figure 5.5 as peaks at 791 cm^{-1} (TO) and 967 cm^{-1} (LO). The solid line in Figure 5.5 represents the contour most frequently recorded for Sample TFB20, which is a signature of the cubic phase. It is worth noticing that both of these specimens were not uniform throughout and, within the laser focusing spot, which in this case was about 1 μm, there were numerous SiC nanowires of different diameters. Fluctuations in the morphology of the specimens in the laser focus account for small variations in the observed spectra.

As seen from the TEM and SEM images in Figures 5.2 and 5.3, SiC nanowires were not aligned but twisted and randomly oriented, and the majority of wires had diameters between 20 and 100 nm. The peak positions observed in Figure 5.5 for Sample TFB20 are shifted from those observed for a bulk crystal of cubic symmetry; 796 cm^{-1} and 973 cm^{-1} for the TO and LO modes, respectively.

Previously, the dependence between Raman peak positions and the size of β-SiC crystals were investigated,[34] and from those results it was estimated that the SiC nanowires in sample TFB20, whose spectra are shown as the solid line in Figure 5.5, are about 30 nm in diameter, which was initially believed to be in very good agreement with the early TEM and SEM data. Crystallite size can also be determined from the angular width of the x-ray diffraction peaks by the Scherrer-Debye method using Equation 2.2 in Chapter 2. The XRD measurements also indicated a crystallite size near 30 nm. The size distribution measurements and subsequent images of the product by TEM and SEM indicate wires with diameters much larger than 30 nm on average. The conclusion drawn from the different size measurements is that 30 nm represents the average distant between stacking fault planes, which from a diffraction standpoint would behave similarly to a crystal edge.

Since there was no unique crystallographic orientation of SiC nanowires in the specimens, the selection rules allow for a small intensity unpolarized LO phonon. Indeed, the LO peak for Sample TFB20 seen in Figure 5.5 is broad and its intensity is relatively small. The intensity of that peak did not change significantly when the focal point was moved to a different location and another cluster of small nanowires was investigated. However, when individual SiC nanowires of diameters about 400 nm were selected, they were oriented with respect to the incident light, and the LO mode peak intensity varied with the relative orientation of the nanowires with respect to the incident light. Figure 5.6 shows spectra of drastically different contours that were recorded for a single nanowire from Sample TFB20 at different focus positions of the incident laser. For some orientations, the LO peak was almost as strong as the TO peak. As pointed out by Frechette and Carraro,[48] the increased LO signal from a single wire relative to a bundle of wires is due to surface phonons.

Raman spectra for Sample CFA64 were also complex. In addition to the peaks due to cubic SiC, the TO and LO phonons characteristic for the hexagonal phase were also observed.

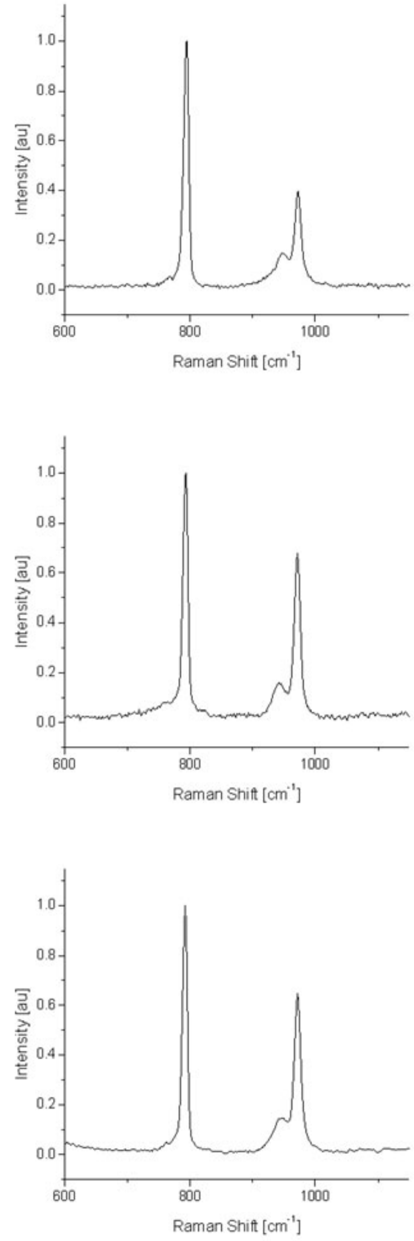

Figure 5.6: Raman spectra recorded by Wieligor[35] at different positions of the incident laser along a single SiC nanowire show that vibrational modes vary with position along the wire.

These phonons were detected at 767 and 938 cm^{-1}. It appears that the hexagonal phase was not a uniform mixture of 2H and 4H structures, as low frequency peaks characteristic for both phases were observed with differing relative intensities at various random locations. Figure 5.7 depicts the spectrum obtained by Wieligor[35] for the case when, within the laser focus, similar concentrations of α and β structures were present. This situation is similar to that recently reported by Cambaz, et al.[49] for SiC whiskers.

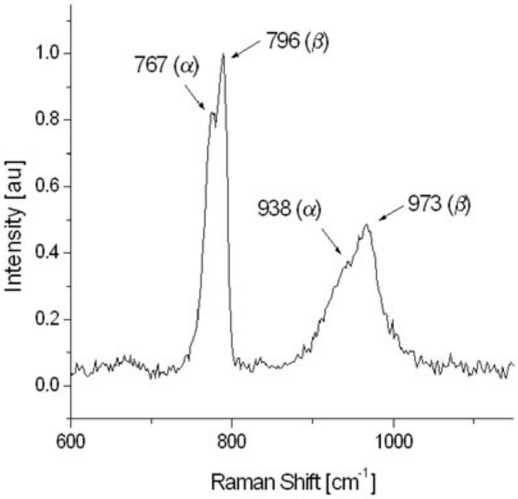

Figure 5.7: This Raman spectrum shows peaks due to both α - SiC and β - SiC.

5.6 Evidence of Stacking Faults

The HRTEM image in Figure 5.3 demonstrates a high concentration of stacking faults in some nanowires. It remains unclear why stacking faults are present in some nanowires and absent in others. Additional examples of stacking faults are depicted in Figures 5.8a and 5.9a.

Frequently, in the TEM images of straight cylinder-shaped wires with diameters as small as about 20 nm, the stacking faults can be observed as dark disks. The mechanism of formation of these shaded areas in relatively low resolution images can be explained as follows. For oblique angles of incidence, when two neighboring cubic domains are separated by a stacking

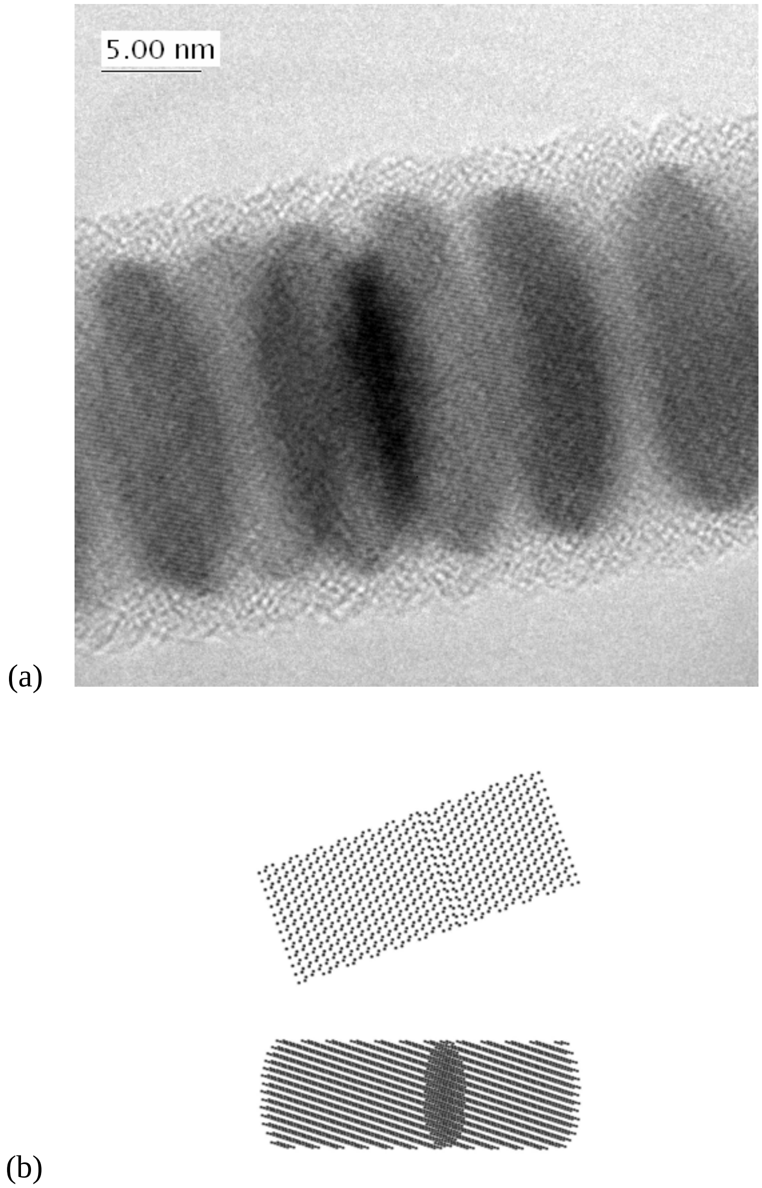

Figure 5.8: (a) High resolution TEM image of stacking faults in SiC nanowires; (b) This atomic model shows why the stacking faults appear as dark lines in the actual sample. The lower image is a simulation of a side view of the stacking fault, while the upper image is the simulated view from the top.

fault, their crystallographic planes are slightly shifted with respect to each other resulting in an apparent increase in the concentration of atoms. This effect shows up as darker, shaded areas on the TEM image, see Figure 5.8b, which depicts top and side views of an atomic model of a cubic structure with a stacking fault. The shape of the ellipsoids depends on the angle between the stacking fault plane and the incident electron beam, compare Figure 5.3. All individual cubic domains depicted in Figures 5.3, 5.8, and 5.9 grow along a single [111] direction, which follows from the fact that all the ellipsoids are perpendicular to the long wire axis. In addition, Figure 5.10 shows clearly that growth (and stacking faults) continue along the [111] even at kinks, bends, and elbows.

Figure 5.9b shows a model cubic structure with one deformation in the form of an ’h’ type plane that separates the nanowire into two crystallites. It is interesting that all of the individual crystallites forming the particular nanowires depicted in Figure 5.9a grew along the [111] direction. In other images numerous twisted wires can be seen. Perhaps those curled nanowires result from the presence of four equivalent [111] directions in the cubic crystal. A change of the path of growth of a nanowire from one to another equivalent [111] direction does not require energy. See for example Figure 5.10. Notice that the stacking faults remain in one direction even as the nanowire twists and bends or curls.

Images from HRTEM showed that the population of stacking faults in small diameter nanowires is greater than in nanowires of diameters about 400 nm. It was possible to observe a section of a thick wire free of stacking faults. This behavior confirms the analysis of Raman band shapes. Bundles of thin nanowires had the TO and LO phonons accompanied by low frequency shoulders of high intensity, but thick isolated, and oriented wires had very low intensity low frequency shoulders, compare Figure 5.6. In Figure 4.19, it is interesting to note that the stacking faults are not necessarily perpendicular to the walls, rather the stacking faults always represent growth along the [111] direction of the crystal.

Stacking faults manifest their presence as shoulders on the low frequency sides of the LO and TO bands in Raman spectra, compare Figures 5.5 and 5.7. Their intensities are directly

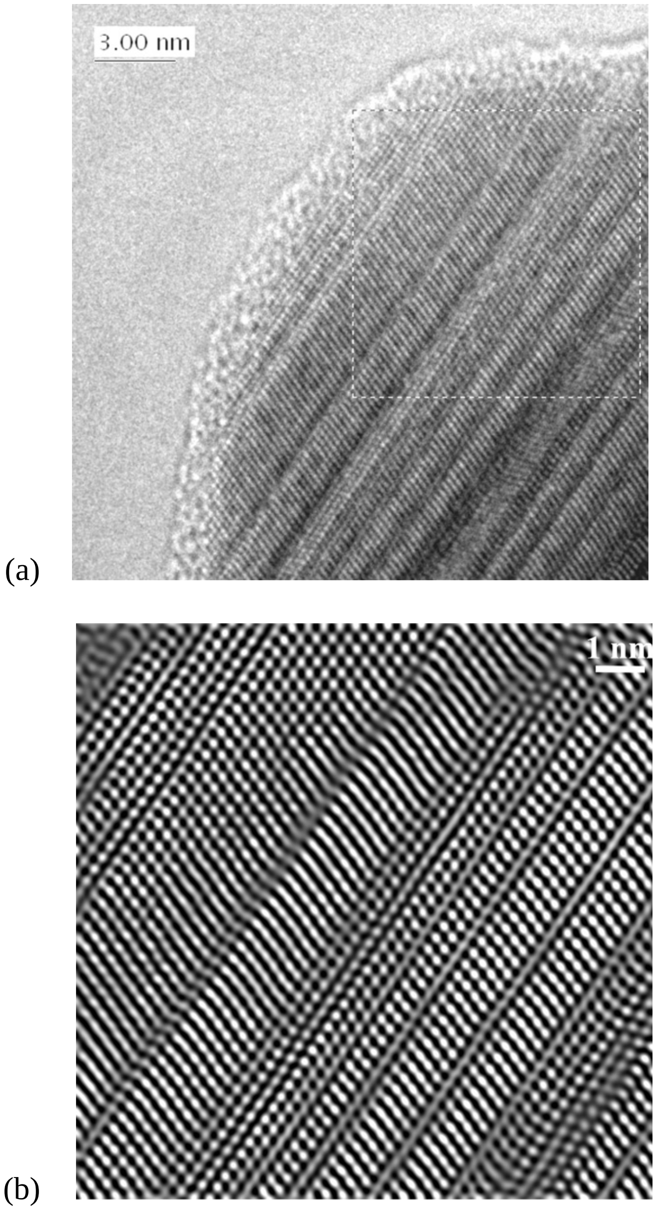

Figure 5.9: (a) Stacking faults are clearly seen in this HRTEM image of SiC nanowires; (b) reconstructed image of the section marked by the dotted line in (a).

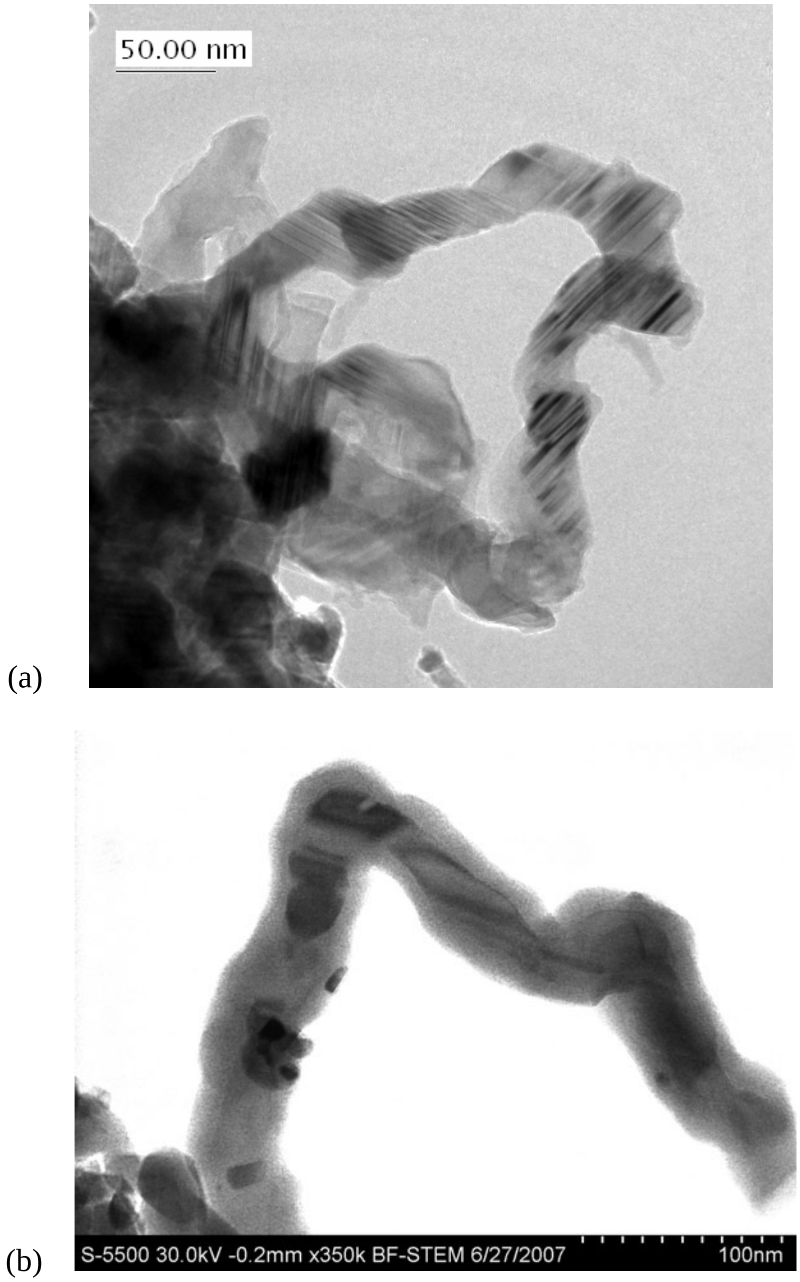

Figure 5.10: (a) In this HRTEM image of CFA64, stacking faults inside the SiC nanowire continue to grow along equivalent [111] directions and (b) at shorter sintering times (3 hours), HRSEM of TFA3 shows that stacking faults are already apparent, and growth along [111] at the kinks and elbows of the nanowire is obvious.

related to the concentration of those defects in the sample. TEM images show that stacking faults are not present in every wire; moreover, it appears that their concentration decreases with increasing diameter of SiC nanowires. These observations explain why Raman spectra of a single wire of about 400 nm diameter had very low intensity shoulders, in contrast to spectra of clusters of nanowires, such as that depicted in Figure 5.5.

Part of the image shown in Figure 5.9a was enhanced by Fourier Transform filtering and individual crystallites can be distinguished in Figure 5.9b. Directions of stacking faults can clearly be seen and the distance between two planes is 0.25 nm, which is the inter-layer spacing between Si-C hexagonal layers. The presence of a broad shoulder near the [111] reflection in the x-ray diffractogram shown in Figure 5.1 is an indication of the presence of stacking faults in the cubic β-SiC structure. Analysis of the shape of this peak may bring additional information on the nature and distribution of stacking faults.[50] A simple twin-like fault corresponds to a single h-type layer inserted in a sequence of cubic c-layers (..cccccc h cccccc..). These faults are demonstrated by a broad peak whose intensity grows with the population of these defects. However, when the frequency of occurrence of the h-type layers (..cccc h c h ccc hh cccc..) increases that shoulder becomes sharper and sharper and eventually looks like a separate peak. Its position corresponds to the [100] reflection of the 2H polytype.[51],[50] The 2H reflection can be observed in the x-ray diffractogram of SiC nanowires in Sample CFA64 shown in Figure 5.1(a). Hexagonal reflections were also noticeable in the XRD of Sample TFB26. However, it is important to add that this peak is not evidence that the 2H phase exists in the specimens, it rather shows that the density of h-type layers is large and randomly distributed throughout the sample. Indeed, Figure 5.9 clearly confirms this observation. In addition, the presence of amorphous SiC can be distinguished near the edges of the nanowires. That layer is estimated to be about 1 nm thick. This value agrees with the infrared data.

Up to now, interior stacking faults and the amorphous surface layer have been discussed only for samples with long sintering times of 20 hours or more. In Chapter 4, it was stated that stacking faults begin to appear in XRD and HRSEM with 3 or more hours reaction time.

Figure 5.11: HRSEM image of TFA8 shows stacking faults inside the SiC nanowire and an amorphous surface layer about 1 nm thick.

Figure 5.11, which is a HRSEM image of Sample TFA8, stacking faults are clearly defined throughout the inside of the nanotube, and the outer surface is amorphous SiO. The x-ray diffraction pattern for this sample shows an obvious shoulder on the [111] SiC peak, see Figure 4.4 in Chapter 4, again confirming the observed stacking faults.

In summary, an indication of the production of stacking faults begins to show as a shoulder on the [111] peak of SiC in XRD after 3 hours of sintering. The HRSEM images confirm that stacking faults begin to appear in the SiC nanowires produced from Sample TFA3. As reaction time increases, the shoulder on the [111] peak becomes sharper, and HRSEM images show more wires with stacking faults, all directed along [111] planes. After 20 hours, the shoulder is sharper, and at 26 hours, the shoulder appears as though it were a separate peak at the position of the [100] reflection of the 2H structure of SiC. HRTEM images continue to confirm that more and more stacking faults are formed as reaction time increases. In addition, Raman spectra include shoulders on the low frequency sides of the LO and TO bands. The intensity of those shoulders increases as the concentration of stacking faults increases. The XRD of the longest reaction time, that of Sample CFA64, shows the most pronounced 2H peak, an indication of an abundance of stacking faults having formed when the reaction is complete, which is confirmed again by HRTEM images and by Raman spectra.

Chapter 6

Conclusions

Nanomaterials are of great interest due to their enhanced physical, mechanical, optical, thermal, electrical, etc. properties. Silicon carbide is of particular interest because it is useful as a semiconductor in electronic applications, and it is widely used for its hardness as a ceramic material to be used in nanocomposites. This study has focused on (1) development of a realistic manufacturing process to produce pure SiC nanowires, (2) understanding the reaction mechanism involved in that production, and (3) studying the morphology and structure of the product.

Induction heating is a safe and efficient method of heating and is also environmentally friendly. In this study, it was found to be a fast and reliable way to produce silicon carbide nanowires from a mixture of silicon nanopowder and multi-walled carbon nanotubes (MWNT). The advantage gained by faster heating and cooling was the reduction of reaction time error down to seconds, thus finding a much more accurate activation energy for this reaction than can be obtained using a conventional furnace, where the error in reaction time is on the order of hours. Burning in air then washing with 30% KOH solution after sintering demonstrates that high purity silicon carbide can be obtained. In addition, if was found that an oxygen-free environment is required, and the geometry and material of the crucible used in the induction furnace must be carefully considered.

The activation energy for the reaction of the mixture of silicon nanopowder and carbon multiwalled nanotubes was found to be 254 ± 36 kJ/mol, which appears to be in conflict with results obtained by Wang,[3] where the activation energy was found to be 96 ± 30 kJ/mol under high pressure. This discrepancy is explained by the difference in the experimental methods used to determine the activation energy. In fact, a comparison of the activation energy found under high-temperature, high-pressure conditions to the results given here confirms that the reaction is diffusion controlled. Under high pressure, particle contact is increased thus requiring less energy to begin the reaction. Additionally, higher temperature provides more energy to the reaction. With the pressure and temperature differences in mind, these results actually do agree with those as well as other published results for similar reactions.[23],[29]

The results of this kinetics study also show that the reaction occurs in one dimension with a decelerating nucleation rate up to the temperature 1325°C. Beginning at 1450°C, 2-dimensional growth was indicated by the value of n, which was confirmed by the observation of individual nanowires fused together to form planar structures at higher temperatures.

The second method of producing pure SiC nanowires was the sublimation of silicon powder in the presence of carbon MWNTs. This method kept any excess silicon separated so that the produced SiC nanowires were pure or included only excess carbon, which was easily removed by burning in air. The reaction began as silicon powder sublimed into the vapor phase and dispersed itself throughout the reaction chamber. As silicon gas contacted carbon layers on the surface of the MWNTs, SiC was produced forming a shell of SiC surrounding a MWNT with carbon layers underneath. Once the MWNTs were completely coated with SiC, further reactions proceeded by both carbon and silicon diffusing through the barrier phase of the product SiC shell.

Growth started at different nuclei, which may have been defects or dislocations in the MWNTs, and proceeded along the walls in both directions. When two growth crystals met, they may have forced a kink or bend in the wire, especially when a stacking fault resulted from the combining of growth from different directions. Different thermal expansion coefficients may have also been a factor in formation of kinks in the nanowires.

The mechanism of formation of these stacking faults is not completely understood, but a few results were clear: (1) the abundance of stacking faults increased steadily with increased reaction time; (2) stacking faults were not present in the earliest formations, which were in fact hollow SiC nanotubes; (3) some wires were completely free of stacking faults, even when the reaction was complete; (4) the stacking faults always represented growth along the [111] direction of the crystal; and (5) the population of stacking faults depends on the quality of the MWNTs.

The structures and the morphology of the product formed showed evidence of (1) solid-vapor reactions that occurred at the outer surface of the nanotubes as silicon vapor reacted with carbon atoms on the surface; (2) solid-solid reactions as silicon vapor condensed and diffused through the outer layer of silicon carbide and reacted with carbon atoms inside the shell to fill the coaxial tube forming solid wires; and (3) vapor-vapor reactions where carbon also sublimed and the vapors reacted to form silicon carbide and then condensed into the flower-like structures observed in many samples. All these results confirm a diffusion-controlled reaction in one-dimension with decelerating or possibly instantaneous nucleation.

Results from x-ray diffraction, TEM, HRTEM, SEM, HRSEM, Raman spectroscopy, and FTIR spectra all demonstrate the validity of this method for producing pure SiC nanowires. The technique is simple, inexpensive, and capable of producing large quantities of SiC nanowires quickly and easily.

The TEM and SEM study allowed the determination of the size and shape of the SiC product. Raman studies confirmed the exact composition of the product and were in agreement with XRD, SEM and TEM results for the crystallite size interpreted to be the mean distance between stacking faults, which was found to be about 30 nm. Analysis of powder x-ray diffractograms indicated the presence of β-SiC with either low concentration of or no dislocations, but clearly indicated stacking faults, which eventually manifest their abundance as a separate 2H peak, indicating how the layers were stacked. The presence of these stacking faults was also confirmed by analysis of Raman spectra, which showed shoulders on the low frequency side of the L0 and T0 peaks that increased in intensity as the concentration of stacking faults increased. The stacking faults indicated by analysis of XRD and Raman spectra were observed in HRSEM and HRTEM images.

All methods were in agreement with the visual data in SEM, HRSEM, and HRTEM images, from which measurements were made to determine the mean diameter of wires sintered for 1 hour and 6 hours. The mean diameter shifted from (59 ± 49) nm up to (113 ± 97) nm as reaction time increased, where the indicated error values are the geometric standard deviation of the distribution. Outer diameter of the largest nanowires continued to grow in time, and the mean diameter shifted to the right, indicating that most nanowires grew in diameter as sintering time increased. More significantly, the width of the distribution increased with increased reaction time, indicating that production by short sintering times allows control of the size of nanowires.

Nanoindentation and AFM could be used to assess the mechanical properties and to describe fine grain structure of the SiC nanowires produced by this method. Thermal atomic vibrations could also be explored to further characterize dimensions and nanostructure of the SiC produced. Better control of partial pressures of silicon vapor might provide better control of surfaces. Further study of those samples produced from precursors single-walled nanotubes (SWNT) and carbon nanograss (CNG) might contribute information on control of microstructure, including stacking faults, or control of alignment of wires, both of which would find useful applications. The results of this additional research would contribute more to the current understanding of the correlation between nanostructure and physical behavior as well as additional information of controlling the formation of SiC nanowires.

Abbreviations

APS	Average particle size
SEM	Scanning Electron Microscopy
HRSEM	Ultra-high Resolution Scanning Electron Microscopy (Hitachi S-4800 and S-5500)
TEM	Transmission Electron Microscopy
HRTEM	High Resolution Transmission Electron Microscopy
XRD	X-ray Powder Diffraction
FTIR	Fourier Transform Infrared Spectroscopy
MWNT	Carbon multiwalled nanotube
SWNT	Carbon singlewalled nanotube
CNG	Carbon nanograss
TF	Tube Furnace
CF	Conventional Furnace
CNT	Carbon nanotubes
MWNT A	Tangled multiwalled nanotubes (carbon)
MWNT B	Aligned multiwalled nanotubes (carbon)
STn	Small radius, thin wall
STk	Small radius, thick wall
LTk	Large radius, thick wall

Bibliography

[1] P. M. Ajayan, L. S. Schadler, and P. V. Braun, *Nanocomposite Science and Technology*, Wiley-VCH, New York, 2003.

[2] E. Y. Alivisatos, A. Paul and Sheng, *Semiconductor Nanocrystal Colloids,* Physics and Chemistry of Nanostructured Materials, Taylor & Francis, Philadelphia, 2000.

[3] Y. Wang and T. W. Zerda, J. Phys.: Condens. Matter **18**, 2995 (2006).

[4] S. Iijima, Nature **354**, 56 (1991).

[5] R. Saito, G. Dresselhaus, and M. Dresselhaus, *Physical Properties of Carbon Nanotubes*, Imperial College Press, London, 1998.

[6] P. B. Amama, B. A. Cola, T. D. Sands, X. Xu, and T. S. Fisher, Nanotechnology **18**, 385303 (2007).

[7] J. J. Romero, IEEE Spectrum: http://spectrum.ieee.org/print/5751 (2007).

[8] M. Park et al., Nanotechnology **17**, 2294 (2006).

[9] C. C. Lin, I. C. Leu, J. H. Yen, and M. H. Hon, Nanotechnology **15**, 176 (2004).

[10] M. Keidar and A. M. Waas, Nanotechnology **15**, 1571 (2004).

[11] B. Cullity and S. Stock, *Elements of X-Ray Diffraction*, Prentice Hall, Upper Saddle River, NJ, 3rd edition, 2001.

[12] G. Will, *Powder Diffraction: The Rietveld Method and the Two Stage Method to Determine and Refine Crystal Structures from Powder Diffraction Data*, Springer, Berlin, Germany, 2006.

[13] Y. Wang, *Silicon Carbide Nanowires and Composites Obtained from Carbon Nanotubes*, PhD thesis, Texas Christian University, 2006.

[14] G. Turell and J. Corset, *Raman Microscopy, Developments and Applications*, Academic Press Limited, London, 1996.

[15] W. Smythe, *Static and Dynamic Electricity*, McGraw-Hill, New York, 3rd edition, 1943.

[16] S. Fahy, C. Kittel, and S. G. Louie, Am. J. Phys. **56**, 989 (1988).

[17] H. Ray, *Kinetics of metallurgical reactions*, International Science Publisher, New York, 1992.

[18] B. S. Bokstein, M. I. Mendelev, and D. J. Srolovitz, *Thermodynamics and Kinetics in Materials Science, A Short Course*, Oxford University Press, Oxford, 2005.

[19] C. Bamford and C. Tipper, *Comprehensive Chemical Kinetics*, volume 22 of *Reactions in the Solid State*, Elsevier Scientific Publishing Co., Amsterdam, 1980.

[20] S. Hulbert, J. Br. Ceram. Soc. **6**, 11 (1969).

[21] J. Latham, *Elementary Reaction Kinetics*, Butterworth, Great Britain, 1962.

[22] B. K. Teo and X. H. Sun, Chem. Rev. **14**, 1485 (2007).

[23] C. Pantea, *Kinetics of Diamond-Silicon Reaction Under High Pressure-High Temperature Conditions*, PhD thesis, Texas Christian University, 2004.

[24] K. L. Wallis, J. K. Patyk, and T. W. Zerda, J. Phys. Condens. Matt (2008 submitted).

[25] M. Avrami, J. Chem. Phys. **7**, 1103 (1939).

[26] M. Avrami, J. Chem. Phys. **9**, 177 (1941).

[27] B. V. Erofeev, C. R. Acad. Sci. URSS **52**, 511 (1946).

[28] V. I. Gorovenko, V. A. Knyazik, and A. S. Shteinberg, Ceramics International **19**, 129 (1993).

[29] C. Pantea et al., Diamond Relat. Mater. **14**, 1611 (2005).

[30] U. J. Kim et al., Phys. Rev. Lett. **95**, 157402 (2005).

[31] A. C. Dillon, T. Gennett, J. L. Alleman, and K. M. Jones, Proceedings of the 2000 doenrel hydrogen program review, 2000 (May 8 -10).

[32] A. Misra, P. K. Tyagi, M. K. Singh, and D. S. Misra, Diamond Relat. Mater. **15**, 385 (2006).

[33] M. Menon, E. Richter, A. Mavrandonakis, G. Froudakis, and A. N. Andriotis, Phys. Rev. B **69**, 115322 (2004).

[34] M. Wieligor, Y. Wang, and T. W. Zerda, J. Phys.: Condens. Matter **17**, 2387 (2005).

[35] K. L. Wallis et al., J. of Nanosci. and Nanotech. **8**, 1 (2008).

[36] X. T. Zhou et al., Appl. Phys. Lett. **76**, 294 (2000).

[37] G. A. Bootsa, N. F. Knippengerg, and G. Verspui, J. Crystal Growth **11**, 297 (1971).

[38] J. Sun et al., Ceramics International **28**, 741 (2002).

[39] H. Dai, E. W. Wang, Y. Z. Lu, S. Fan, and C. M. Lieber, Nature **375**, 769 (1995).

[40] T. Taguchi, N. Igawa, H. Yamamoto, S. Shatamo, and S. Jitsukawa, Physica E **28**, 431 (2005).

[41] Y. Sasaki, Y. Nishima, M. Sato, and K. Okamura, Phys. Rev. B **40**, 1762 (1989).

[42] H. Mutschke, A. C. Andersoen, D. Clement, T. Henning, and G. Peiter, Astron. Astrophys. **345**, 187 (1999).

[43] H. Mutschke, T. Henning, D. Clement, and A. C. Andersen, arXiv: astro-ph/0111301 v2 ASP conference series (2001).

[44] M. I. Baraton and M. S. El-Shall, Nanostructured Materials **6**, 301 (1995).

[45] G. Compagnini, G. Foti, and A. Makhtari, Europhysics Lett. **41**, 225 (1998).

[46] L. Geng and J. Zhang, J. Mat. Chem. Phys. **84**, 243 (2004).

[47] S. Rohmfeld, M. Hundhausen, and L. Ley, Phys. Rev. B **58**, 9858 (1998).

[48] J. Frechette and C. Carraro, Phys. Rev. B **74**, 161404(R) (2006).

[49] G. Z. Cambaz, G. N. Yushin, Y. Gogotsi, and V. G. Lutsenko, Nano Lett. **6**, 548 (2006).

[50] S. Stelmakh, B. Palosz, and S. Gierlotka, Mat. Sci. Forum **228**, 663 (1996).

[51] B. Palosz, S. Stelmakh, and S. Gierlotka, Z. Kristallographie **210**, 731 (1995).

Vita

Personal Background

Kendra Lee Wallis, Arlington, Texas
Daughter of Kenneth Wayne Wallis & Irma Jeanne Wallis
Married Michael Zane Brand, June 5, 1993
Two Children, Megan Jeanne O'Neall - Age 20
Zoe Christine Wallis - Age 11

Education

Texas Christian University
Ft. Worth, TX
Ph.D., Physics 2008

University of Texas at Arlington
Arlington, TX
M.S., Physics 1993

West Texas A&M University
Canyon, TX
B.S., Physics with Math Minor 1985

Employment History

Lecturer in Physics, UTA, 8/02 - Present
Graduate Teaching Assistant, TCU, 8/04 - 12/07

Publications

Stacking Faults in SiC Nanowires
K.L. Wallis, M. Wieligor, T.W. Zerda, S. Stelmakh, S.Gierlotka, B.Palosz
J. Nanosci. Nanotechnol., **8**, 1 (2008)

Reaction Kinetics of Nanostructured Silicon Carbide
K.L. Wallis, J.K. Patyk, T.W. Zerda
J. Phys.: Condens. Matt., (2008) submitted

Conference Presentations

Texas Section APS Meetings
Stacking faults in SiC nanowires
Reaction Kinetics of Nanostructured Silicon Carbide

Professional Memberships

American Physical Society
American Association of Physics Teachers
National Science Teachers Association
Physics Instructional Resource Association
American Association of University Professors

ABSTRACT

PRODUCTION AND CHARACTERIZATION OF NANOSTRUCTURED SILICON CARBIDE

by Kendra Lee Wallis, Ph.D., 2008
Department of Physics and Astronomy
Texas Christian University

Dissertation Advisor: T. Waldek Zerda, Professor of Physics and Chair of the Department

Nanostructured materials continue to attract attention because of their new and interesting properties, which are very different from their macrostructured equivalents. Since the size of grain and surface differs, a better understanding of the microstructure, the mechanism of formation, and methods of controlling surface properties is necessary.

In this study, nanostructured silicon carbide has been produced from the solid-solid reaction of a mixture of silicon nanopowder and carbon multiwalled nanotubes (MWNT) sintered by induction. A study of the reaction rate at different temperatures has yielded a value for the activation energy of 254 ± 36 kJ/mol, and has led to the conclusion that the reaction is diffusion-controlled.

A second method produced pure silicon carbide nanowires using a procedure which kept the solid reactants, silicon powder and MWNT, separated while sintering at a constant temperature of 1200°C. Silicon in the vapor-phase reacted at the surface of the MWNTs followed by diffusion of both precursors through the product phase boundary.

The reaction time was varied, and a morphological study has been done describing changes in shape and size as a function of time. The initial reaction produced a layer of SiC providing the outer shell of coaxial structures with carbon nanotubes inside. As Si and C diffused through the product phase to react at the interface, the tube became filled with SiC to form solid SiC nanowires, and the outer diameter of the nanowires grew continuously as reaction time in-

creased. After long sintering times, growth continued in two dimensions, fusing nanowires together into planar structures.

In addition, the precursor form of carbon was varied, and nanowires produced by two different types of nanotubes have been studied. The produced SiC nanowires show cubic crystal structure. After a few hours of sintering, stacking faults began to occur inside the wires, and the frequency of occurrence of the stacking faults increased as reaction time increased. Long sintering times from 26 to 64 hours produced enough stacking faults to manifest as a 2H peak in x-ray diffractograms. HRTEM and HRSEM showed evidence of an amorphous phase at the surface about 2 to 3 nm thick.